Silk fibroin hydrogels and films for neurological applications

A Thesis

Submitted by:

Thomas McShea Valentin

In partial fulfillment of the requirements for the degree of

Master of Science

In

Biomedical Engineering

TUFTS UNIVERSITY

MAY 2013

Abstract

Silk fibroin is a unique biomaterial that can be processed into numerous different physical states, that can be used for applications such as drug delivery, tissue engineering, and optics. This thesis explored two new neurological applications for silk fibroin biomaterials that could lead to significant advancements in drug / gene delivery and *in vitro* models of brain injury.

First, silk fibroin hydrogels were optimized to create a biomimetic brain phantom in a traumatic brain injury model using a mixture of silk fibroin hydrogels and 200μm silk fibroin fibers. These hydrogels were able to mimic the biomechanical properties of mouse and rat cortical tissue in confined compression (~50 kPa), and were able to match the rheological properties (dynamic viscosity and dynamic shear modulus) of these cortical tissues within the physiological range for traumatic brain injury (~20 kPa in the range of 60-100 rad/s). In addition, these hydrogels exhibited the same diffusivity properties as cortical tissue. Cell encapsulation studies were also briefly explored and showed promising initial results.

Second, silk fibroin films were explored for their drug and gene delivery capabilities. Therapeutic necrostatins were loaded into silk fibroin films and delivered to the mouse cortex in a controlled cortical impact traumatic brain injury model to explore the ability to inhibit injury-induced necroptosis. Additionally, adeno-associated viral vectors were loaded into similar silk films and delivered to the cortex of mice to explore transduction of sub-dural cortical neurons, and dural fibroblasts for potential disease model targets such as meningioma.

Acknowledgments

I would first like to thank the most important people in my life: my parents Melissa and Vince, who have never stopped believing in me and by whose example I can credit most of my successes, my sisters Celine and Natalie without who life would not be as enjoyable as it is today. They are without doubt my best friends and I am beyond grateful for how close of a relationship we all maintain. I also want to thank my grandparents Jim McShea, and Pierre and Marie-Jose Valentin for all their generosity and support in helping me grow. I also want to thank all of my friends over the years who have been there to enjoy all of the time we spent together, and who helped keep me sane and grounded.

I would chiefly like to thank Dr. David Kaplan for all of the opportunities he has given me over the past 4+ years during my undergraduate career and through my time as a graduate student. I could never have dreamed such an amazing mentor existed. Eleanor Pritchard was also instrumental in shaping the researcher I have become. Without her excellent example, I would not have gained the motivation and passion for research that I have today.

I would also like to thank my advisors Gary Leisk and Catherine Kuo and my collaborators Michael Whalen and Casey Maguire. Your guidance and help throughout has been instrumental in getting me here. To all of my colleagues at Tufts, Dr. Min Tang-Schomer, Dr. Jelena Rnjak, Amy Hopkins, Lee Tien, Dr. Jon Kluge, Steph McNamara, Dan Graziano, Tory Gray and Dr. Rosalyn Abbott, I am indebted to you for all of your help over the years.

Thank you all.

Table of Contents

❖ List of Figures

with Alexa Fluor® 594. Silk film with AAV9 and DMSO with dura intact.

Figure 30 Immunostaining of cortical sections illustrating dural transduction using AAV9-loaded (3.85×10^{10} g.c./film) silk films. No duratomy performed prior to film implantation. Scale bar = 100μm. Reproduced with permission from Dr. Min Tang-Schomer. 60

❖ List of Tables

❖ List of Abbreviations

TBI	Traumatic Brain Injury
PTSD	Post-traumatic Stress Disorder
DAI	Diffuse Axonal Injury
EB	Evans Blue
PDMS	Polydimethylsiloxane
CCI	Controlled Cortical Impact
FITC	Fluorescein Isothiocyanate
Nec-1	Necrostatin-1
Nec-3	Necrostatin-3-FITC
PI	Propidium Iodide
AAV	Adeno-associated Virus
CNS	Central Nervous System
AAV8	Adeno-associated Virus Serotype 8
AAV9	Adeno-associated Virus Serotype 9
GFP	Green Fluorescent Protein
DMSO	Dimethyl Sulfoxide
FPLC	Fast Protein Liquid Chromatography

Chapter 1. Silk Fibroin as a biomaterial

Silk has a long history of use as a suture material that goes back thousands of years. As a biomaterial it is considered biocompatible (does not cause an inflammatory reaction) and biodegradable (degrades naturally *in vivo*) making it a good candidate for multiple applications. Any biomaterial should satisfy the following criteria:

1. Causes little or no inflammatory or toxic reaction,
2. Resorbs completely in a timely, controllable fashion, and
3. Sufficient mechanical, chemical and physical properties to support the tissue.

One of the biggest attractions of silk is that it can be processed and formulated to satisfy all of the above criteria.

Silk fibroin exists in two main forms: virgin, pre-spun silk fibroin is referred to as Silk I, and the processed and/or crosslinked silk is referred to as Silk II. Silk 1 is water soluble but also very unstable. When exposed to shearing forces, drawing, heating or spinning (as when a spider spins a web) it is irreversibly converted to Silk II. The β-sheet structure of Silk II is more energetically favorable than that of Silk I. An electrical current can also reversibly convert Silk I to Silk II depending on the direction of the current book [4]. This conformational change results in an extension of the chain lengths and an 18.3% decrease in protein separation distance which makes it more water insoluble as the water is now excluded from the spaces between the protein chains [5]. The insolubility of silk II and the smaller inter-chain distances make it essentially invulnerable to water, dilute acids/alkali, chaotropes (urea, guanidine hydrochloride), most organic solvents and many proteolytic enzymes.

Silk II fibroin, as it is spun by insects, needs to be processed in order to be converted back into the Silk I form which is typically needed for it to be used in the vast majority of biomaterial applications. The processing protocol involves first de-gumming the silk (sericin removal) through boiling in a 0.02M sodium bicarbonate solution [Figure 1]. The silk fibers are then solubilized in a 9.3M lithium bromide (LiBr) solution followed by dialysis in water to remove the LiBr, leaving only the solubilized silk fibroin [5].

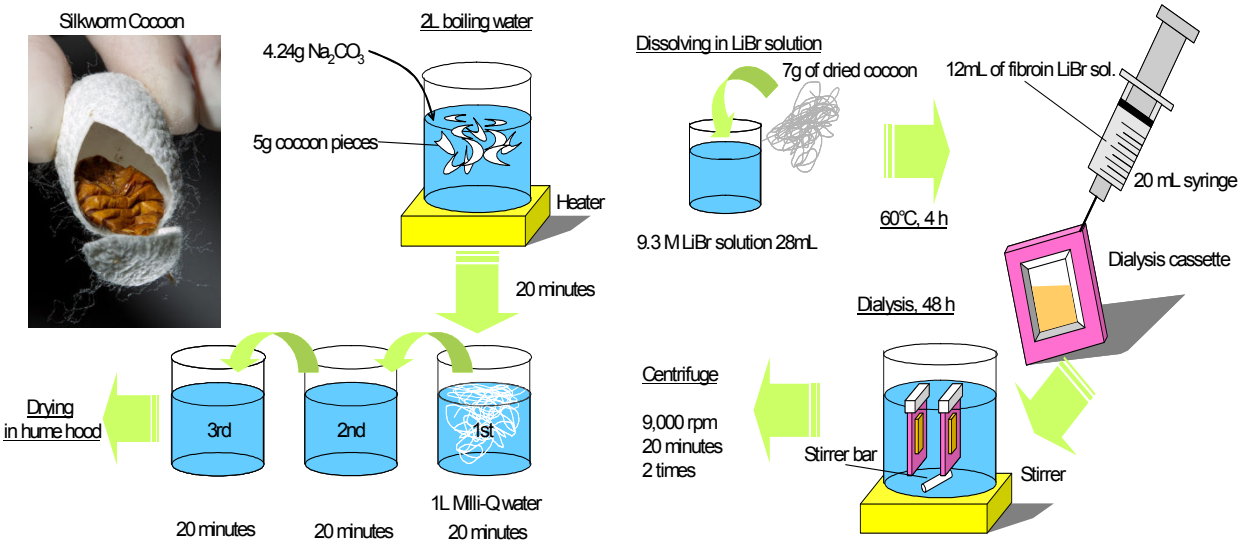

Figure 1 Cartoon of silk fibroin processing showing sericin removal from *Bombyx mori* cocoons and subsequent LiBr dissolution and dialysis. Silk cocoon image: http://www.nytimes.com/slideshow/2011/03/07/science/08SILK.html

The biomedical potential of silk arises from silk II being reverted back into the pre-spun silk I conformation through the resolubilization process. Resolubilized silk is much more hydrophilic and water soluble enzymes, drugs, protease inhibitors, etc. can be dissolved into the aqueous silk solution for numerous drug delivery applications. The aqueous silk solution can then be crosslinked mechanically, electrically, chemically or through water vapor annealing back into the silk II form. Mechanical crosslinking can be done using ultrasonication or vortexing [6, 7]; electrical crosslinking can be done by inserting two oppositely charged probes into the silk solution which will then reversibly form a hydrogel around the positively charged probe [4];

chemical crosslinking can be done with a highly concentrated salt solution [8-15] or methanol [16-19]; and water vapor annealing is done in a vacuum chamber [20-22]. The process of crosslinking the silk locks in the β-sheet structure and entraps the solute in a way that stabilizes and protects the solute (e.g. prevents covalent coupling of enzymes, decreases in antibiotic activity, prevents unfolding or denaturing of encapsulated proteins, etc.). Crosslinking also essentially locks in the physical structure of the silk, allowing for numerous different physical conformations such as brittle films [16-22], hydrogels [4, 6, 7, 23-27], porous sponges [8-15], electrospun mats [28-34], and microspheres [35-39]. Crosslinking also increases the degradation life of the silk substrates due to an increase in hydrophobicity [5].

The degradation of silk has been extensively studied both *in vivo* and *in vitro* [15, 40, 41]. *In vitro* studies showed that degradation of silk is possible using Protease XIV, Collagenase IA, α-chymotrypsin and Protease XXI but Protease XIV was the most successful at uniformly degrading the silk [40]. Protease XIV non-discriminately cleaves the protein chains into smaller particles (0.1-2.4 kDa, but most range from 0.1-0.5 kDa) and continues to further break down the

Table 1 Amino acid composition ($^{g}/_{100g}$) of degradation products of porous silk fibroin sheets exposed to α-chymotrypsin, collagenase-IA and Protease XIV. Adapted from [38].

	Concentration in degradation solution after 9 days of exposure ($^{g}/_{100g}$)		
Amino Acid	**α-chymotrypsin**	**Collagenase IA**	**Protease XIV**
Lysine	3.92	4.13	1.19
Histidine	–	–	–
Arginine	3.92	2.16	2.25
Aspartic Acid	13.73	–	0.24
Threonine	3.92	1.38	1.42
Serine	7.84	0.39	2.49
Glutamic Acid	7.84	5.11	0.71
Proline	–	1.77	–
Glycine	19.61	12.76	11.61
Alanine	13.74	11.98	26.61
Cysteine	–	13.56	18.74
Valine	7.84	8.25	1.41
Methionine	1.96	3.14	10.56
Isoleucine	3.92	3.54	1.19
Leucine	3.92	7.66	3.08
Tyrosine	3.92	9.63	15.66
Phenylalanine	3.92	14.54	3.20

particles over time. All of the aforementioned agents degrade the silk into its constituent amino acids [Table 1] [41]. These amino acids are readily resorbed by the body which prevents a long term immune reaction. *In vivo* degradation studies also illustrated a weaker immune response with silk over other established biomaterials such as poly(lactic acid) and collagen [17].

These biomaterial properties have made silk fibroin an ideal choice for numerous biomaterial applications. Using different processing techniques, silk fibroin can be cast into various different shapes, while retaining biocompatibility and biodegradable abilities. This goal of this thesis was to explore silk fibroin's ability to mimic the biomechanical properties of brain tissue, and to allow for controlled, sustained release of therapeutic drugs and gene delivery vectors.

Chapter 2. Silk Fibroin hydrogels as a biomimetic brain tissue phantom

A. Introduction

Traumatic brain injury (TBI) is an increasingly important health issue with at least 10 million TBIs occurring annually around the world [42]. In the United States alone, 1.4 million people suffer a TBI each year, resulting in 1.1 million emergency department visits, 235,000 hospitalizations, 80,000 permanent severe neurological disabilities, and 50,000 deaths [43-45]. In addition, with the onset of the Unites States led wars in Iraq and Afghanistan, there has been a significant surge in the number of combat-related TBIs. These are strongly linked with post-traumatic stress disorder (PTSD) and other problems such as depression and impaired cognitive function [46]. Because the exact mechanisms and pathophysiology of TBI have not been fully explored, accurate TBI models are necessary to further our understanding. Currently, there are three major paradigms of TBI in animals and are classified as Impact Acceleration Models, Inertial (non-impact) Acceleration Models, and Direct Brain Deformation Models [47].

Impact acceleration models consist of direct cranial impacts with a piston, captive bolt pistol, pendulum or weight drop and have been used in primates [48-53], sheep [54-57], cats [58], rats [59-61], mice [62-67] and rabbits [68]. Inertial acceleration models involve angular acceleration of the head without acute impact, and generally generate more consistent results as compared to linear acceleration models [47]. Inertial acceleration-related TBIs are also significantly more destructive as they lead to diffuse axonal injury (DAI) from the resultant shear forces [**Table 2**]. DAIs consist of widespread axonal damage throughout the parasagittal white matter of the cerebral cortex, corpus callosum, and the pontine-mesencephalic junction

Table 2 Summary of applicable TBI Models (Adapted from [47]). *DVS = Rate of Death, Vegetative survival, or Severe disability in hospitalized TBI patients [87, 88].

Model type	Primary TBI Damage	Secondary TBI Damage	%DVS*	Mechanical Model
Impact linear acceleration	Focal · Vascular injury · Axonal injury · Contusion · Laceration	Focal · Focal hypoxic-ischemic injury · Focal brain swelling	8-10%	Confined compression: stress-relaxation
Inertial angular acceleration	Diffuse · Diffuse axonal injury · Diffuse vascular injury	Diffuse · Diffuse hypoxic-ischemic injury · Diffuse brain swelling	42%	Parallel-plate rheology

near the superior cerebellar peduncles [69-71]. Inertial acceleration models have been used in primates [72-77], pigs [78-80], cats [81], rabbits [68], and rats [82-86].

This goal of this project is to establish a silk fibroin hydrogel brain phantom that could accurately model both Impact Acceleration and Inertial Acceleration Models of TBI *in vitro*. In order to make the model as accurate as possible, it would additionally mimic the drug diffusion properties of small molecular weight dyes, which could allow for development of an *in vitro* TBI brain phantom with encapsulated neurons. An *in vitro* brain phantom made from silk fibroin hydrogels would allow for rapid prototyping of novel TBI models in a reproducible manner and without the need for the maintenance of animal models.

Hydrogel brain phantoms have thus far been limited to catheter perfusion studies or used to establish 3-dimensional computerized models of the brain. Hydrogel brain phantoms have typically been made using various biomaterials such as 0.2-0.6% agarose [89-92] and gelatin [93-95] for positive-pressure catheter infusion-related studies, and poly(vinyl alcohol) [96, 97] for MRI and ultrasound modeling. Computerized models for TBI are excellent for studying the mechanics of TBI, but they can only predict possible outcomes. A living *in vitro* model would be able to empirically generate data on actual cell response to TBI.

This study proposes using silk fibroin as a biomaterial to create an aqueous hydrogel that accurately mimics the mechanical and diffusive properties of brain tissue. Silk fibroin hydrogels have been extensively characterized [23, 98] and can be formed via ultrasonication (used in this study) [6], vortexing [7] and electrogelation [99]. Silk hydrogels have also been used for cell encapsulation of human mesenchymal stem cells [6]. Combined with the ability seed cells within the hydrogel [6], these hydrogels can be cast into any potential shape and will accurately mimic the mechanical viscoelastic properties of brain tissue while encapsulating cortical neurons. Through testing a range of different hydrogel configurations and by optimizing each property, the specific aims of this study were to,

1. Accurately mimic the compressive properties of cortical brain tissue in confined compression
2. Accurately mimic the rheological properties of cortical brain tissue in dynamic shear and dynamic viscosity
3. Accurately mimic the diffusivity properties of small molecules into *in vivo* cortical brain tissue
4. Encapsulate cortical neurons and promote cell survival

The sonicated silk hydrogel brain phantom used in this study optimized the mechanical properties of the hydrogel to match that of mouse brain tissue in a confined compression stress-relaxation test. The viscoelastic properties (dynamic complex modulus and dynamic viscosity) were also optimized against those of mouse brain tissue, along with the passive diffusion of 960 MW Evans Blue dye though the hydrogel / brain tissue.

B. Materials & Methods

1. Silk Fiber Preparation

Silk fibers were prepared using *Bombyx mori* silkworm cocoons supplied by Tajima Shoji Co (Yokohama, Japan) and following the established protocol that has been successfully used to create silk fibers through hydrolysis [100]. The cocoons were degummed by boiling in a 0.02M sodium carbonate solution for 20 min, washed in deionized water and air dried.

Sodium hydroxide pellets weighing 3.5g were added to 5 ml of distilled water to obtain a 17.5M solution. When approximately 70% of the NaOH pellets had been dissolved, 0.35g of the dried silk was added and stirred with a spatula for 180 seconds. To stop the hydrolysis reaction, 45 mL of water was added and the fibers were then centrifuged at 3,500 rpm for 5 minutes. The supernatant was discarded and the fibers were resuspended in 50 ml of purified water, stirred and centrifuged again 5 to 8 times in order to remove excess remaining alkali. The pH of the solution was then adjusted to 7.0 using hydrochloric acid. The neutralized fiber solution was once again centrifuged at 3,500 rpm for 5 minutes and resuspended in water (repeated 3-5 times). Finally, the fiber solution is lyophilized.

2. Silk Hydrogel Preparation

Silk solution was prepared from *Bombyx mori* cocoons as outlined in previous studies [9, 11, 28, 101, 102]. The cocoons were boiled for 20m, 30m and 45m, in a 0.02M sodium carbonate solution, rinsed three times with distilled water and dried overnight. The extracted silk fibroin was then dissolved in a 93M LiBr solution at 60°C for 4 hours. The solution was then dialyzed in distilled water using Slide-a-Lyzer dialysis cassettes (MWCO 3500, Pierce) for 2 days to remove the LiBr from the solution.

To suspend the silk fibers in the hydrogels, the silk fibers were first suspended in purified water, and then added to the concentrated silk solution to yield a final concentration of 4% (w/v)

200μm silk fibers in a 4% (w/v) silk fibroin solution. This solution was then sonicated using a Branson Digital Cell Disruptor ultrasonification system for 20s at 20% amplitude.

For the confined compression studies, 3mL of the sonicated silk solution was transferred to a 3.5cm-diameter petri dish to yield hydrogels with a height of approximately 2.5mm. For the confined compression stress-relaxation model, the hydrogel samples were designed to have an aspect ratio of 2:1 (5mm diameter, 2.5mm height). To decrease gelation time, the dish was then wrapped in Parafilm and placed in a 60^0C oven for 1-3 hrs or until fully gelled. Once gelled, a 5mm-diameter biopsy punch (VisiPunch Dermal Biopsy Punch, Huot Instruments) was used to punch out the hydrogels. Hydrogels were then stored in a 10cm-diameter petri dish with purified water to prevent desiccation.

For rheological studies, 4mL of the sonicated silk solution was transferred to a 5cm-diameter petri dish to yield gels of approximately 2mm in height. The dish was then wrapped in Parafilm and placed in a 60^0C oven for 1-3 hrs or until fully gelled. Once gelled, a 10mm-diameter biopsy punch was used to punch out the hydrogels. Hydrogels were then stored in a 10cm-diameter petri dish with purified water to prevent desiccation.

For EB diffusion studies, 1mL of the sonicated silk solution was pipetted into a 2mL eppendorf tube, sealed and placed in a 60^0C oven for 1-3 hrs or until fully gelled. The diffusion studies would take place in the eppendorf tube. At each time point, selected gels would be removed from the tubes and sacrificed for imaging and analysis.

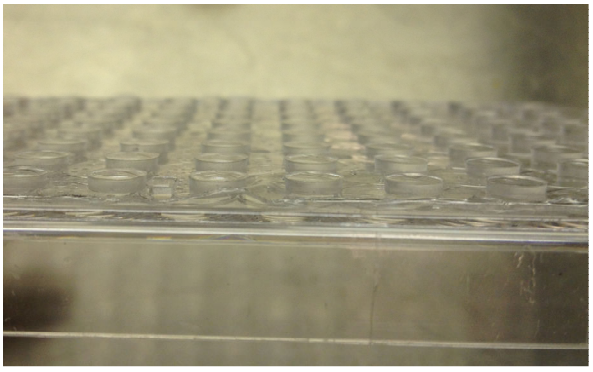

Figure 2 PDMS mold for casting silk fibroin films.

3. Silk Film Preparation

Silk solution was prepared from *Bombyx mori* cocoons as outlined in the previous section.

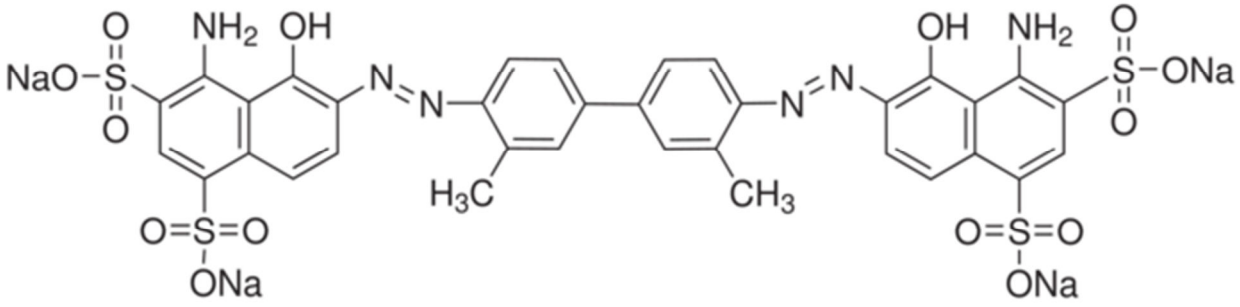

Figure 3 Chemical structure of evans blue dye (Sigma-Aldrich).

The purified silk solution was diluted to 2% (w/v), and 10 mg/mL Evans Blue (EB) (Info) was mixed in gently by inversion. A Polydimethylsiloxane (PDMS) mold was cast with raised 5mm-diameter cylinders in an 8 x 12 pattern [Figure 2]. 13μL of the EB / silk solution was pipetted onto each raised cylinder and spread with a pipette tip to cover the entire surface of the cylinder. Films were rendered water insoluble by introduction of β-sheets through water-annealing in a vacuum for 3 hours in the presence of a water source at room temperature [103-105]. After water annealing, films dried and carefully lifted from the PDMS mold using a scalpel and forceps. The films were stored at room temperature and protected from light.

4. Agarose Hydrogel Preparation

0.6% (w/v) Agarose hydrogels were prepared according to [89-92]. The 0.6% agarose solution was heated to speed dissolution of the agarose. For confined compression studies, 3mL of the agarose solution was transferred to a 3.5cm-diameter petri dish to yield hydrogels with a height of approximately 2.5mm. The dish was then wrapped in Parafilm and stored at 4^0C until fully gelled. Once gelled, a 5mm-diameter biopsy punch (VisiPunch Dermal Biopsy Punch, Huot Instruments) was used to punch out the hydrogels. Hydrogels were then stored in a 10cm-diameter petri dish with purified water at 4^0C to prevent desiccation.

For rheological studies, 4mL of the agarose solution was transferred to a 5cm-diameter petri dish to yield gels of approximately 2mm in height. The dish was then wrapped in Parafilm

and stored at 4^0C until fully gelled. Once gelled, a 10mm-diameter biopsy punch was used to punch out the hydrogels. Hydrogels were then stored in a 10cm-diameter petri dish with purified water at 4^0C to prevent desiccation.

5. Collagen Hydrogel Preparation

Collagen hydrogels were prepared from Collagen I from rat tail (BD), 10X 199 medium (Gibco) and 1M NaOH. Gels were prepared with 88% (v/v) collagen I, 10% (v/v) 10X 199 media, and 2% (v/v) 1M NaOH. For rheology studies, 500µL of collagen hydrogel placed on a 12mm diameter coverslip and incubated at 37°C until fully gelled and transferred onto the rheometer platens before testing. The collagen gels were too structurally weak to be loaded into the confined compression fixture.

6. Brain Tissue Sample Preparation

Whole mouse brains were collected from 6-10 week old, female balb/c mice post-mortem (sacrificed via CO_2 asphyxiation). The brains were immediately removed, stored in chilled phosphate buffered saline solution, and tested immediately. For confined compression studies, a 5mm-diameter biopsy punch (VisiPunch Dermal Biopsy Punch, Huot Instruments) was used to punch out the appropriately sized samples from the cortex, which were then trimmed to approximately 2.5mm in height using a scalpel. For rheological studies, a 10mm-diameter biopsy punch was used to punch out the samples from the cortex, which were then trimmed to approximately 2mm in height using a scalpel.

7. Confined Compression Testing

A customized confined compression setup was machined using aluminum stock (McMaster Carr) [Figure 5] and 40μm pore size Ultra-Fine Filtering Type 316L Stainless Steel Porous Discs (McMaster Carr) [Figure 5]. The 5mm hydrogels were placed in the bottom hole of the aluminum collar, which was then carefully inverted and placed on top of the aluminum rod containing the filter discs. An Instron mechanical tester was used for confined compression. The stress-relaxation test was performed by slowly lowering the indenter at 0.1% compressive strain / sec. until the load cell registered 0.05 kgf. At this point the gauge length of the sample was zeroed and the sample was compressed at a rate of 0.1% compressive strain / sec. to 5% compressive strain. At this point the indenter position was held in place for 500 seconds, to allow for equilibrium of the sample. The sample was then compressed an additional 5% of the initial gauge length and equilibrated until the sample had been compressed by 35% compressive strain. Rapid impact was avoided due to the aqueous nature of these hydrogels. Under rapid compression the sample does not have time to equilibrate and the registered modulus will be dominated by the effects of water (an incompressible fluid) being forced out of the small pores in the hydrogel. By allowing for equilibration, the modulus registered will be of the

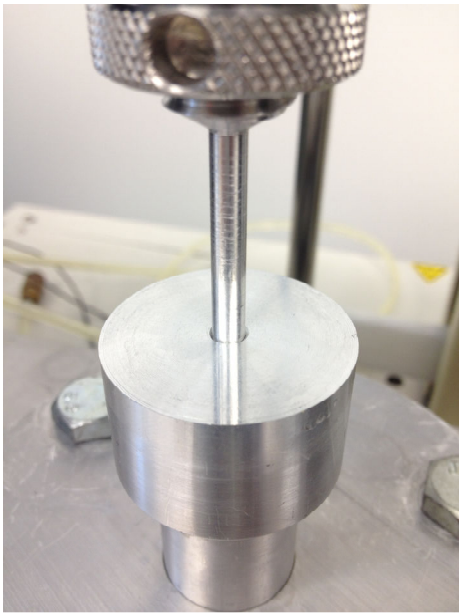

Figure 5 Confined compression set up constructed from aluminum sock.

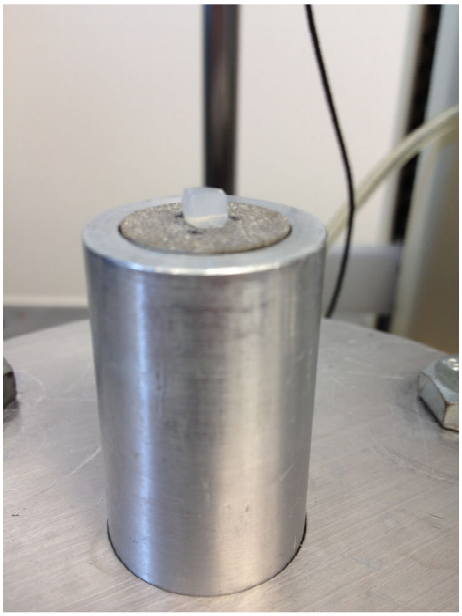

Figure 5 Ultra-fine porous steel filtering disc used for drainage of water from the samples during equilibrium.

hydrogel itself instead of the water.

8. Rheology

Two 25mm-diameter parallel plate geometries (TA Instruments) were used and augmented with Very Fine 220 Grit Stick & Sand® adhesive sandpaper (Norton Abrasives, Niagara Falls, NY) that had been trimmed to 25mm-diameter circular sections. The 10mm-diameter hydrogels were placed in the center of the platens with the help of a customized acrylic plastic guide designed for sample alignment [Figure 7]. The platens were then lowered to a ≤ 2mm gap with the normal force remaining within 1-5 g·cm [Figure 7]. Frequency sweeps were performed from 1-100 rad/s at a controlled 1% strain and at room temperature. Strain sweeps were performed from 0.1-100% strain at a controlled 5 rad/s frequency and at room temperature.

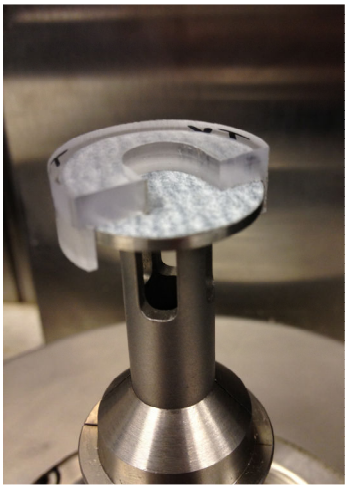

Figure 7 Acrylic plastic (PMMA) guide for sample alignment.

Figure 7 Loaded sample with platens at nominal gap of ≤ 2mm.

9. Cell Encapsulation

Silk hydrogels for cell encapsulation studies were prepared by suspending the fibers in the silk solution in the same manner as for the mechanical tests. In order to aid with cell adhesion to the hydrogels, 0.04% (w/v) Rat Tail Collagen I (BD) was added to the hydrogels. After addition of the collagen, the hydrogels were sonicated for 10 sec. at 15% amplitude. Primary neuron cultures (Provided by the laboratory of Dr. Steve Moss, Tufts Medical Center for Neuroscience) were then added at such a concentration to yield approximately 100,000 cells per well. 50µL of ungelled silk hydrogel was then added to a well of a 96 well plate. The cell-loaded gels were then incubated at 37°C and 5% CO_2. The increased temperature in the incubator speeds gelation of the silk hydrogels. At 1 day

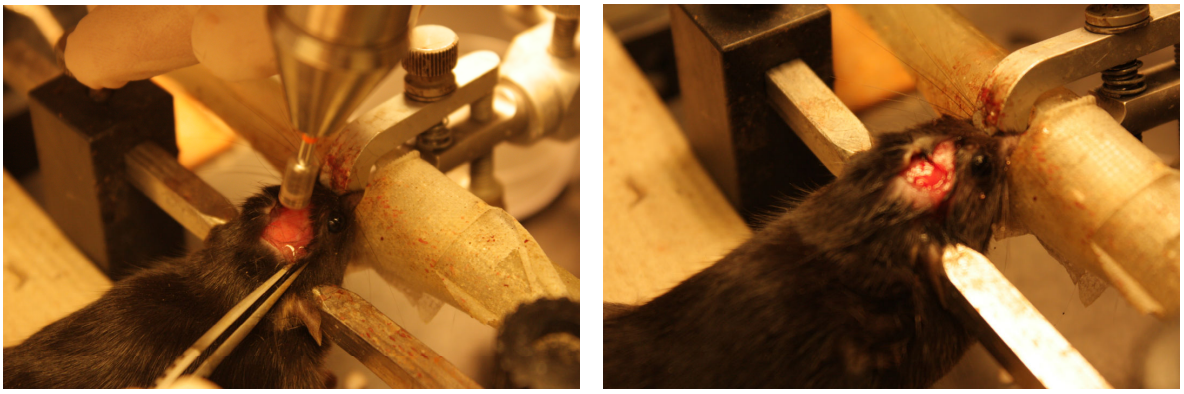

Figure 8 Craniectomy is first drilled using a 4mm hole saw, being careful not to damage the dura mater or brain tissue below. Once drilled, the bone flap is removed with forceps. After placing the silk film on the surface of the brain, the bone flap is replaced and the incision is stitched closed.

and 4 day time points, a Live/Dead assay was performed and imaged using confocal microscopy (Leica).

10. Hydrogel Diffusivity

Silk hydrogels with varying fiber concentrations were prepared in 2 mL eppendorf microcentrifuge tubes as previously stated. Once gelled, an EB-loaded silk film was placed on top of the hydrogel in the center, and the eppendorf tube sealed and stored at 37^0C. At each time point, hydrogels were sacrificed by removing the hydrogel from the eppendorf tube and cutting it in half using a scalpel. The cross-section of the hydrogel was then imaged and processed using Image J (National Institutes of Health) to quantify penetration depth into the hydrogel.

11. *In vivo* Diffusivity

In vivo diffusion of Evans Blue was done using a mouse animal model in accordance with the protocol (2004N000286) approved by the Massachusetts General Hospital Institutional Animal Care and Use Committee and is compliant with the NIH Guide for the Care and Use of Laboratory Animals. Mice were anesthetized using isoflurane, an incision was made through the scalp and a craniotomy was performed using a 4mm-diameter surgical hole saw. Following the craniotomy, EB-loaded silk films were placed on top of the dura mater of mice and the bone flap replaced on top of the film [Figure 8]. At each time point, subject mice were sacrificed by

Table 3 P-Value Summary		
P-Value	**Significance**	**Marker**
< 0.001	Extremely Significant	***
0.001 – 0.01	Very Significant	**
0.01 – 0.05	Significant	*
> 0.05	Not Significant	

anesthesia with isoflurane followed by decapitation. The brains were recovered, cryo-sectioned and imaged using a fluorescence microscope through a Texas Red filter. Images were processed using Image J (NIH) to measure penetration depth into the brain at each time point.

12. Statistics

All statistics were performed using GraphPad Prism. The significance of each sample vs. mouse brain tissue was calculated using a 1-way Dunnett ANOVA test at each sampling point and then averaged. The average significance of each sample in the relevant physiological rangeof ω = 60-100 rad/s (applicable to published values for angular velocity or frequency (ω) in animal TBI models) was calculated for the dynamic shear modulus. For the aggregate modulus study, the significance of each sample vs. mouse brain tissue was calculated using a 1-way Dunnett ANOVA test. For the EB Diffusion study, the significance of each sample vs. mouse brain tissue was calculated using a 1-way Dunnett ANOVA test. For all tests in which statistics were performed, the average statistical summary is listed in the corresponding graph legend.

C. Results & Discussion

1. Rheology

4% (w/v) silk hydrogels with 3-5% (w/v) fibers were tested in both a frequency sweep to analyze the dynamic shear modulus [Figure 12] and strain sweep to analyze the dynamic viscosity [Figure 13]. Mouse brain tissue, as well as four control hydrogels [6% (w/v) silk with no fibers, 4% (w/v) silk with no fibers, 0.6% (w/v) agarose, and collagen] were also tested under the same experimental conditions. The dynamic shear modulus properties of these silk hydrogels are consistent with previous rheological studies [61]. By inspection, the different fiber concentrations had no significant effect on the rheological properties. The limiting factor appears to be the overall silk concentration in the hydrogel. While the brain tissue samples have a different frequency-dependence than the silk hydrogels, they both appear to align in the higher frequency range (ω=60-100 rad/s). These values are consistent with the physiological range of published values for angular velocities used for *in vivo* animal models of diffuse TBI that successfully induced DAI [Table 4]. This suggests that within the range used to induce TBI, the 4% silk hydrogels accurately mimic brain tissue. Within this range, the dynamic shear modulus of the 6% silk hydrogels is significantly higher than both the 4% hydrogels and the brain tissue. Additionally, the dynamic shear moduli of both agarose and collagen control hydrogels are significantly lower than that of the 4% silk hydrogels and the brain tissue samples.

Table 4 Published values for angular velocity in animal TBI models.

Angular Velocity ω (rad/s)	Source
138	
118	
104	
82	
78	[106]
78	
61	
59	
56	
96	[107]
138	[108]

A similar result is seen with the dynamic viscosities for 4% silk hydrogels and brain tissue. Over the strain sweep, the dynamic viscosities for the 4% hydrogels and brain tissue samples are broadly similar as compared to the 6% silk hydrogels, as well as the agarose and

collagen hydrogels. One future direction could explore the effects of cerebrospinal fluid (CSF) in the hydrogels instead of water. There is a chance that a fluid like this could affect the rheological properties of the hydrogels. The effect of CSF in silk hydrogels has not yet been explored and it is unknown whether or would change the beta sheet formation or other properties of the hydrogel, but this would be another potential area of exploration.

2. Confined Compression

An initial study of varying silk hydrogels was performed with boil-times of 20m, 30m and 45m. The goal of this was to identify whether boil time had an effect on mechanical properties. Figure 14 shows that 30m boil time silk at a concentration of 4% (w/v) had the most desirable mechanical properties. Based on these results, 30m boil time 4% (w/v) silk hydrogels were chosen for further fiber-reinforcement studies. 3-5% (w/v) 200μm fibers were suspended in the hydrogels and evaluated in confined compression [Figure 15]. A stress-relaxation test was performed and was water was allowed to flow out through a porous steel disc underneath the hydrogel during equilibration between compression steps. Brain tissue samples from mice and rats as well as agarose hydrogels were tested in the same conditions.

Stress relaxation tests consist of a series of compression steps, followed by an extended relaxation period before the next compression step. During this equilibrium step, the indenter is held at the same position and water is allowed to flow out of the sample. The purpose of this is to allow for equilibrium of the sample. Fluid dynamically, water is considered an incompressible fluid so the resistance of the water that is trapped within the hydrogel dominates the forces measured by the transducer during the compression step. By allowing for equilibrium, the compressed water is allowed to exit the hydrogel and whatever force is measured at the end of the equilibrium period is the force exerted by hydrogel matrix itself. Figure 10 illustrates the compressive force over time. Figure 10 shows the compressive load vs. compressive strain. The

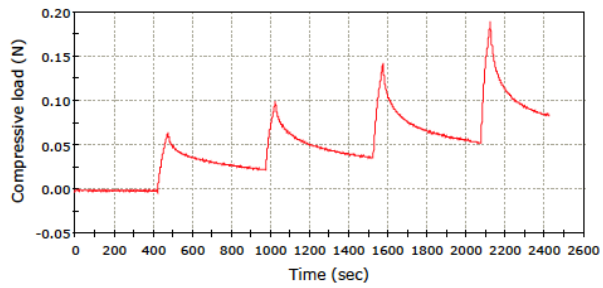

Figure 10 30m boil time, 4% (w/v) silk hydrogel. Compressive load over time shows the asymptotic leveling-out of the compressive load during equilibrium.

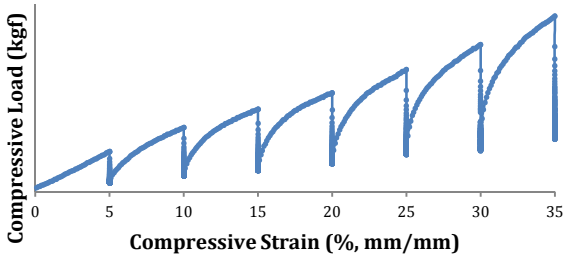

Figure 10 30m boil time, 4% (w/v) silk hydrogel. Compressive load vs. strain shows minimum load after equilibrium. The slope of the regression of these minima is converted to the aggregate modulus of the hydrogel.

peaks represent the compression step (stress), which is quickly followed by the sample returning to its equilibrium state (relaxation) which is represented by the local minima. The minimum force registered during each relaxation/equilibrium period is then plotted. A linear regression of the minima on the compressive load vs. compressive strain graph [Figure 10] is then obtained and the slope of these equilibrium points is converted into the Aggregate Modulus (H_A) for that particular sample.

The compressive properties of the hydrogels used in this study are consistent with the results from previous studies [6, 23]. The aggregate modulus of the 4% fiber hydrogels was almost identical to both types of cortical brain tissue, where as the 5% fibers were significantly above, and the 0% fiber hydrogels, 3% fiber hydrogels, 2% silk hydrogels and the 0.6% agarose hydrogels were all significantly below the cortical brain tissue. This shows that the fiber-reinforced 4% hydrogels are significant closer to the actual aggregate modulus of cortical brain tissue than other published brain phantom models.

The results of this study are similar to the rheology studies in that the major contributing factor for mechanical properties appears to be the overall silk concentration in the hydrogel. Unlike with the rheology tests where the fiber concentration had an insignificant effect on

mechanical properties, in confined compression the fiber concentration has a significant effect and can be used to fine-tune the aggregate modulus to match that of the tissue of choice.

Possible reasons for the significant change of modulus in hydrogels without fibers compared with that of hydrogels with fibers included, could be that the fibers have altered the beta sheet structure of the hydrogel during crosslinking. One method that this could be examined would be with FTIR spectroscopy. This would be able to detect any altered beta sheet formation immediately surrounding the fibers and it would be possible to form a hypothesis as to whether or not this could be responsible for the change in modulus.

3. Diffusivity

EB diffusion through the hydrogels showed that the silk hydrogels containing 200μm fibers controlled the diffusion of EB through the hydrogel significantly. When compared to the diffusion of EB in an *in vivo* animal model, the rate of diffusion in both fibrous silk hydrogels and in *in vivo* brain tissue were broadly identical, as compared to non-fibrous silk hydrogels and agarose hydrogels [Figure 16]. Similarly with the confined compression studies, there is a chance that the fibers changed the beta sheet structure of the hydrogel and that some EB became trapped in this modified beta sheet, which limited its diffusion. These are observations that could also be made using FTIR spectroscopy. These results indicate an ability of these hydrogels to allow for small-molecule drug diffusion into the hydrogel at a similar rate to that of brain tissue.

4. Cell Encapsulation Studies

The goal of incorporating live neurons and astrocytes into this brain phantom model was to create a living brain phantom that could give *in vitro* feedback of TBI in ways that mechanical models cannot. There are numerous cell-based assays that could be used to analyze the extent of cell damage as a result of a TBI. The benefit of using silk hydrogels as a matrix is they can be cast in almost any shape and have been shown to successfully encapsulate hMSCs. Early preliminary results showed that these fiber-reinforced hydrogels could successfully encapsulate neurons and astrocytes for up to 4 days [Figure 11]. After these promising initial results, a full-scale study was attempted numerous times to repeat these results but this either yielded unimpressive results or for unknown reasons the cells did not survive. Due to time availability, the cells had been isolated many hours prior to encapsulation and the extended period of incubation time in a high concentration of cells may have proved fatal. Another possibility is that the concentration of the silk hydrogel along with the fibers and collagen may have been too much for the cells to survive.

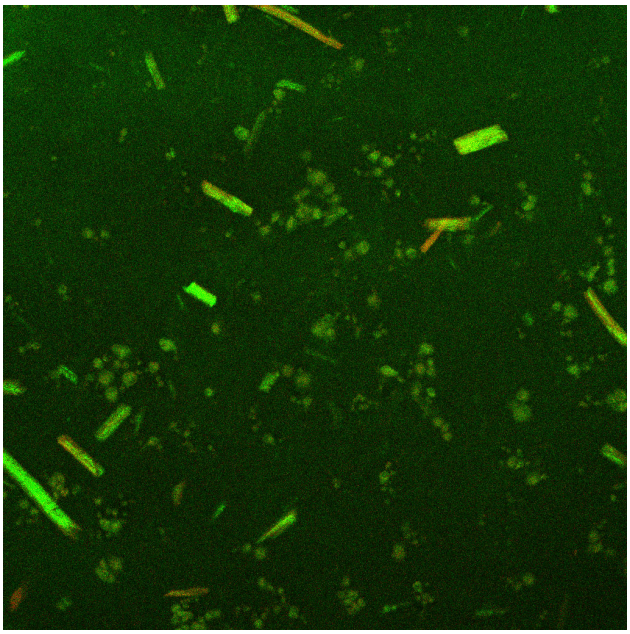

Figure 11 Confocal microscopy of a fiber reinforced silk hydrogel with 0.04% collagen after 4 days of culture in neurobasal medium. Live / Dead stains were incubated for 12 hours overnight in order to allow for diffusion into the hydrogel. The brighter, rectangular shapes are the silk fibers that have absorbed the Live stain.

D. Conclusions

Silk fibroin, already known used in countless biomaterial applications, has now been shown to be an excellent biomaterial for a biomimetic brain phantom. The numerous methods in which silk hydrogels can be customized to alter their mechanical properties make it an ideal choice for future studies seeking to establish biomimetic phantoms of other tissue types. By taking advantage of boil

time (30m), silk fibroin protein concentration [4% (w/v)], fiber length (200μm) and fiber concentration [4% (w/v)] it was possible to create a brain tissue phantom with the same mechanical properties in compression and shear as well as diffusivity. These results have shown that it is possible to create a hydrogel that can be optimized to the same mechanical and diffusive properties of cortical brain tissue, and previous studies have illustrated the ability of silk hydrogels to successfully encapsulate cells. Future directions could combine the proven ability of these 4% (w/v) hydrogels to encapsulate cells to create a living brain phantom.

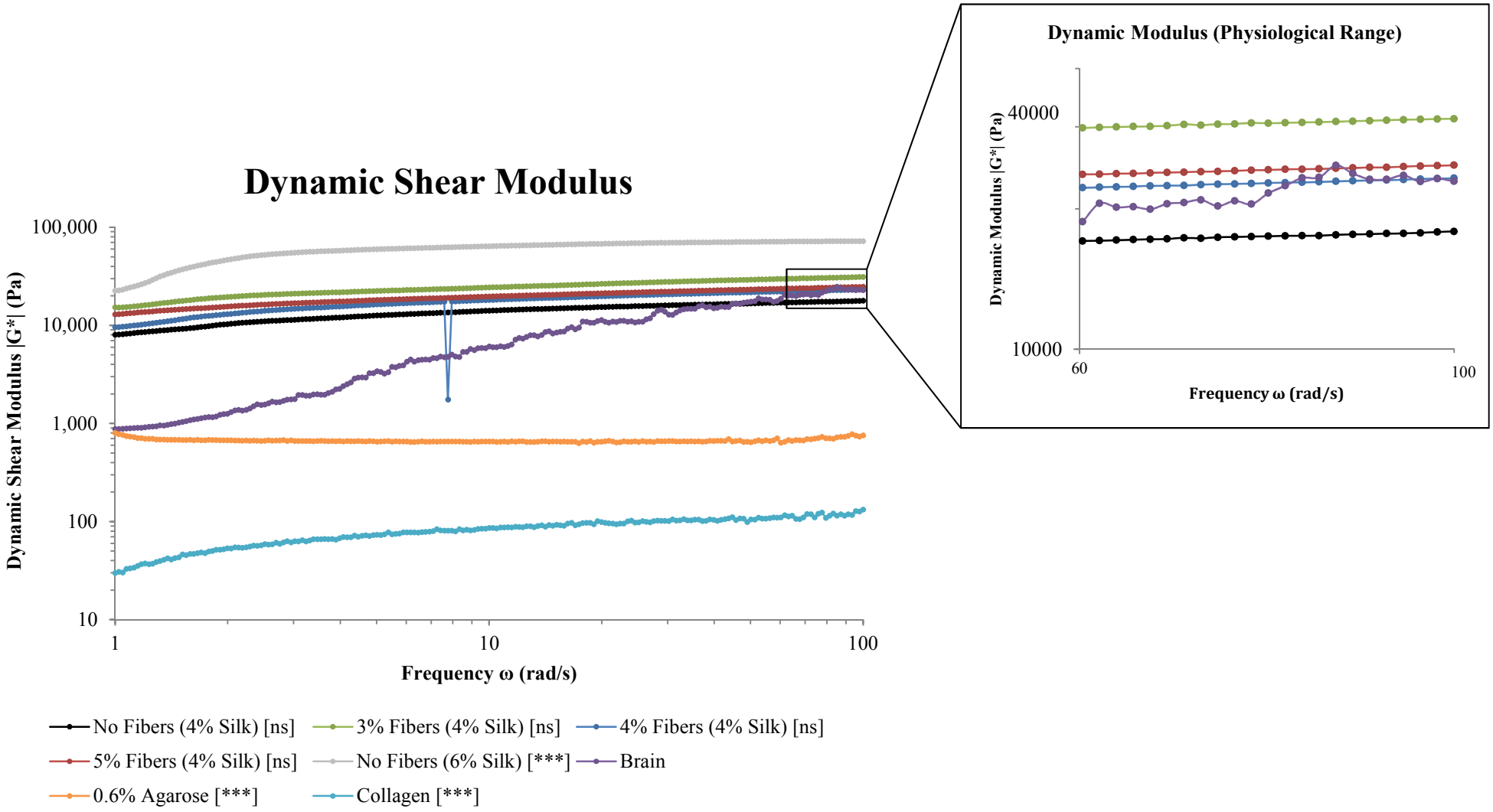

Figure 12 Frequency sweep for the Dynamic Shear Modulus at constant strain (ε = 1%). Silk control hydrogels (4% and 6% silk with no fibers), 0.6% Agarose and Collagen hydrogels were compared against fibrous hydrogels and brain tissue. Within the physiological range (ω = 60-100 rad/s), 6% silk, 0.6% agarose and collagen hydrogels were all extremely significantly different from brain tissue. Within the physiological range, all 4% silk hydrogels (including fibrous hydrogels) were all statistically similar (no significant difference) to brain tissue.

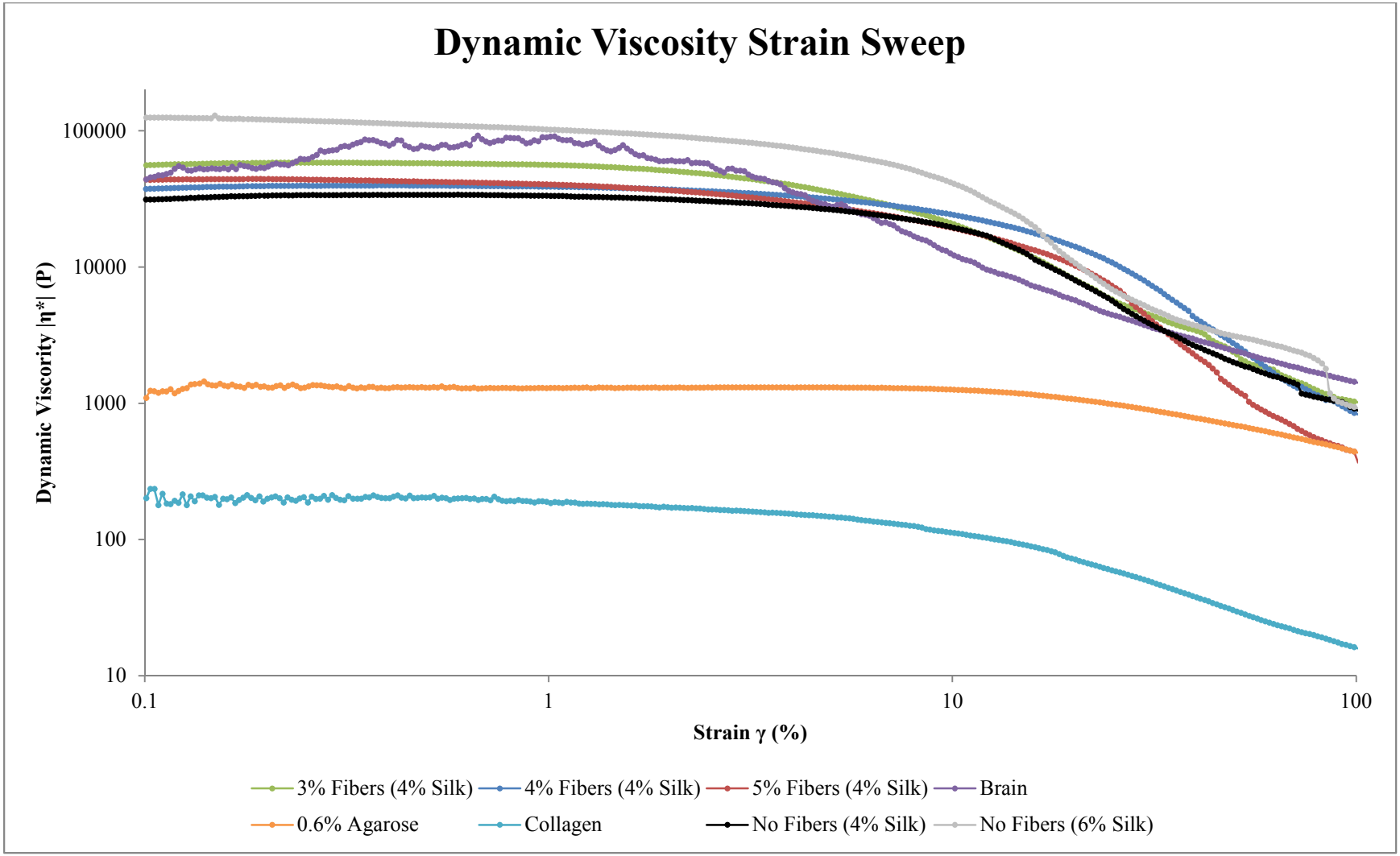

Figure 13 Strain sweep for the Dynamic Viscosity at constant frequency (ω = 5 rad/s). Strain-dependent viscosity responses of 4% Silk hydrogels (including fibrous hydrogels) are broadly similar to that of brain tissue. 0.6% agarose and collagen hydrogels are orders of magnitude less viscous than the silk hydrogels and brain tissue.

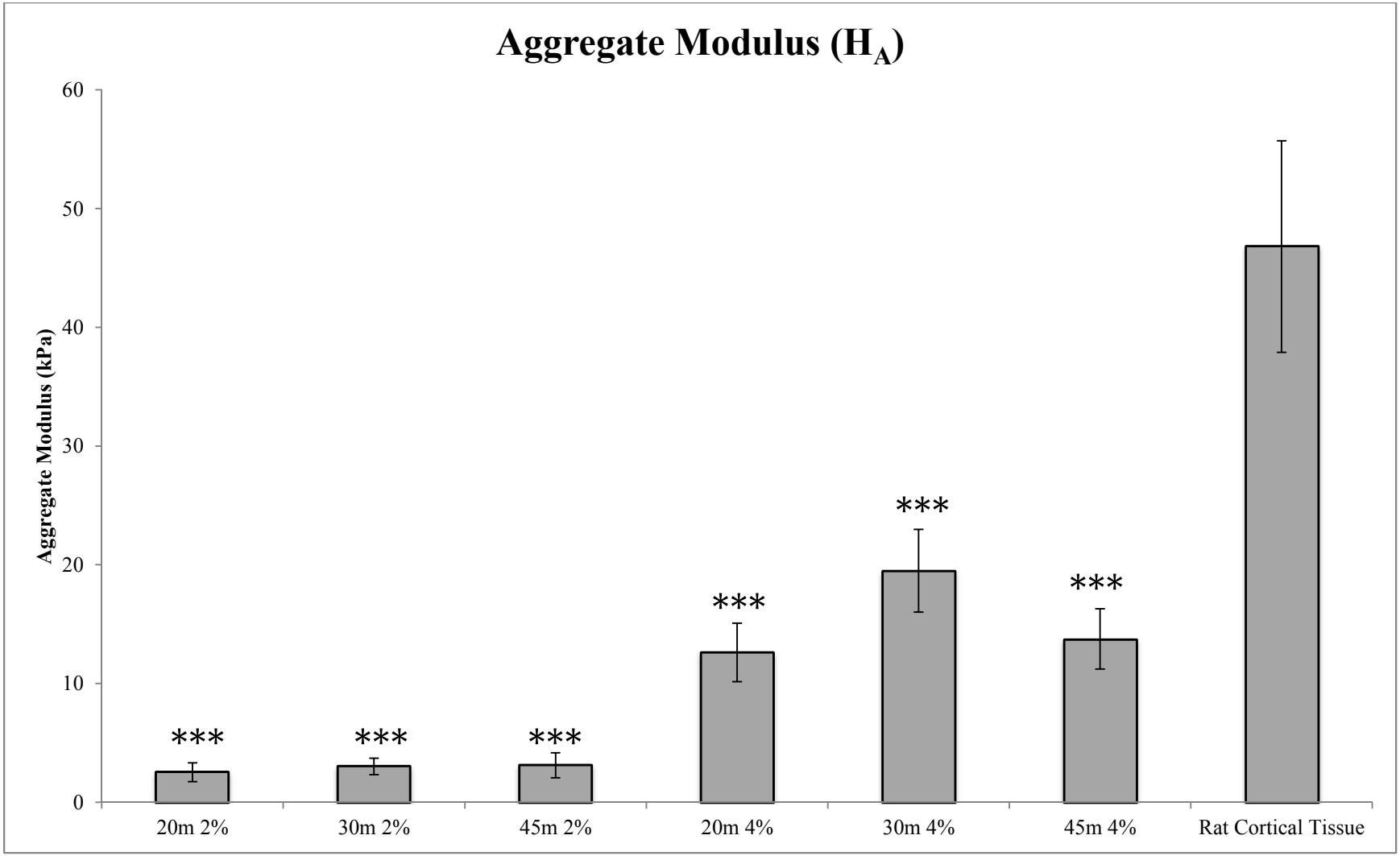

Figure 14 Aggregate modulus as observed during a stress-relaxation confined compression test. 3 different boil times at two different concentrations each were tested in order to gather a baseline for potential candidates. It was determined that 30m boil-time silk was the best candidate to move forward with fiber-reinforcement studies.

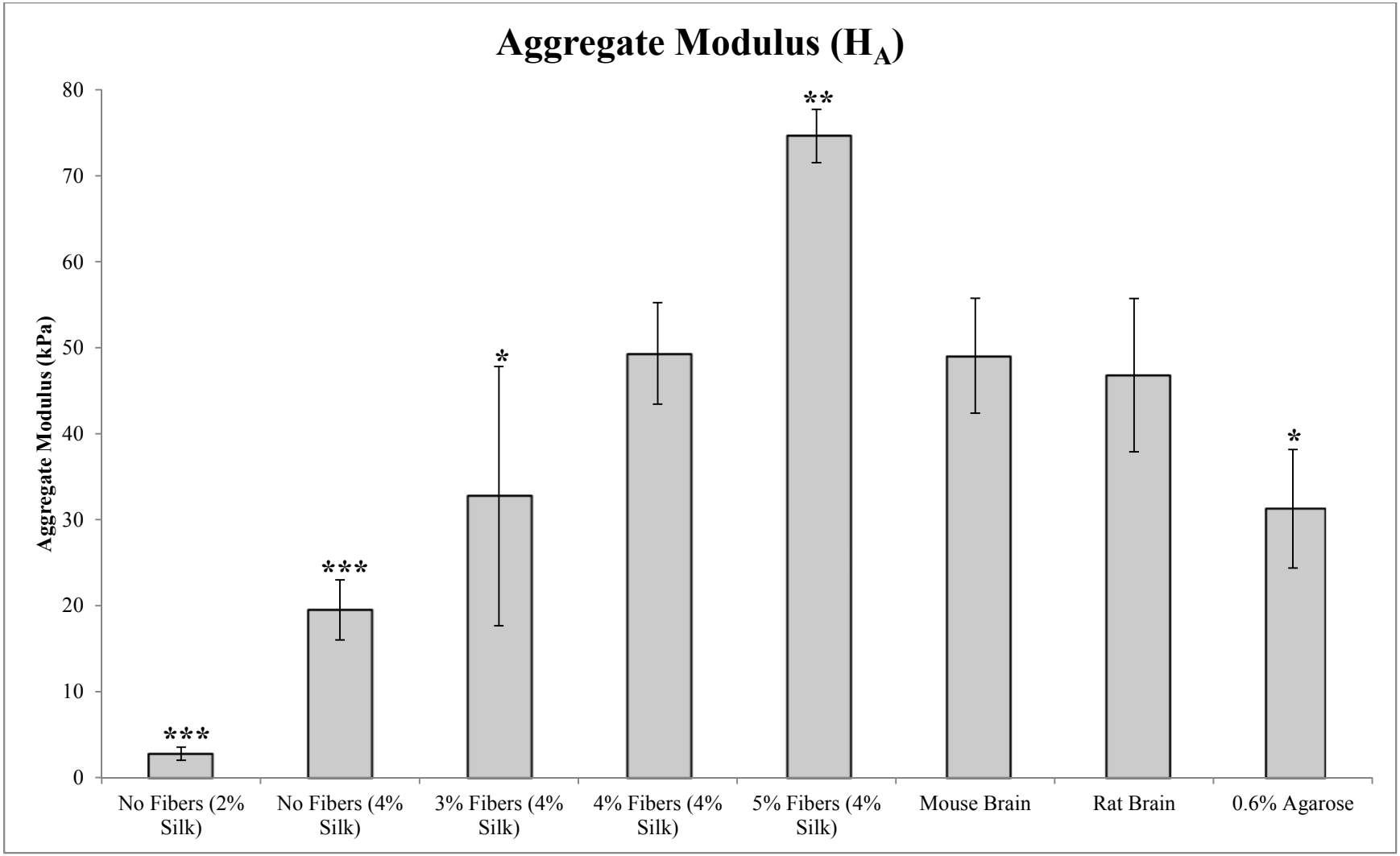

Figure 15 Aggregate modulus as observed during a stress-relaxation confined compression test. 30m boil-time 4% silk hydrogel with 4% fibers was statistically similar to both brain tissue sample groups. All other hydrogels, including 3% and 5% fiber hydrogels, were statistically different from brain tissue.

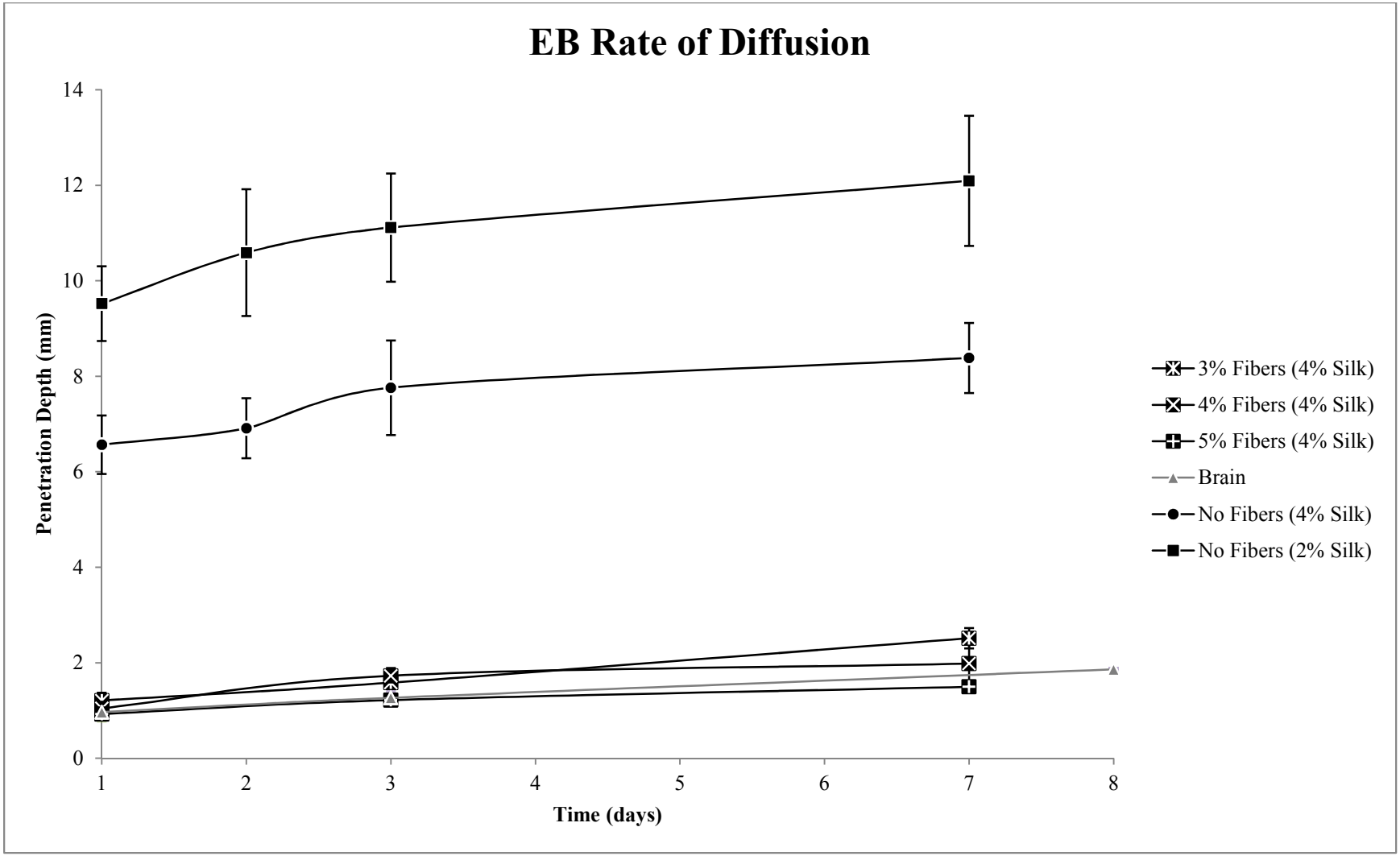

Figure 16 Evans Blue diffusion penetration depth over time. 200μm fiber silk hydrogels had diffusion rates broadly similar to that of *in vivo* brain tissue, whereas non-fibrous silk hydrogels and agarose hydrogels had much higher rates of diffusion.

Chapter 3. Silk Fibroin films for controlled delivery of therapeutic drugs

A. Introduction

One of the most frequently used *in vivo* models of TBI is the controlled cortical impact (CCI) model, which is a type of Impact Acceleration Model mentioned in Chapter 2 [1-3]. It has been used extensively to examine the mechanisms of TBI in mouse models [64, 66, 109-113]. Using a CCI mouse model, this study proposes to use the drug delivery abilities of silk fibroin substrates to explore potential therapeutic solutions for TBI. The benefit of this technology is that it does not require any additional procedures in the case of severe TBI. In severe TBI, a craniectomy is generally performed in order to relieve pressure on the brain from swelling due to trauma. This application would allow for the drug-loaded film to be placed on top of the brain during this procedure, without requiring any additional procedures since the dura mater / cortex would already be exposed. In addition, due to the very thin profile of these films, they would not exert any additional pressure on the brain when the craniectomy is replaced. Silk films are also biodegradable and therefore would degrade over time *in vivo* [15, 40, 41].

Controlled, localized drug delivery is advantageous in this application because it would avoid global administration of therapeutic drugs throughout the body, making it much more effective and allowing for a more concentrated delivery to the wound site. Global administration requires a much larger delivery dose due to clearance by the kidneys or liver, and uptake by other tissues in the body. This would be avoided with a drug-loaded film that would be placed directly over the wound site.

The CCI model chosen in this study uses a CCI device to impart a linear impact onto the cortex of anesthetized mice. The CCI device [Figure 17] is a stroke-constrained pneumatic impactor. The device consists of a stroke-constrained cylindrical stainless steel pneumatic impactor with a 5.0 cm stroke length. The cylinder is mounted vertically on an adjustable crosshead. The impactor tip consists of a short aluminum rod measuring 9 mm diameter and 1.50 cm in length, with a flat face and a rounded (2.0 mm radius) perimeter edge. For each trial, the impactor cylinder shaft with the impactor tip in place is extended the full stroke length. The crosshead holding the cylinder is then lowered until the impactor tip compresses the dura and underlying subdural space. This is used as the zero position from which the depth of the CCI is controlled. The cylinder

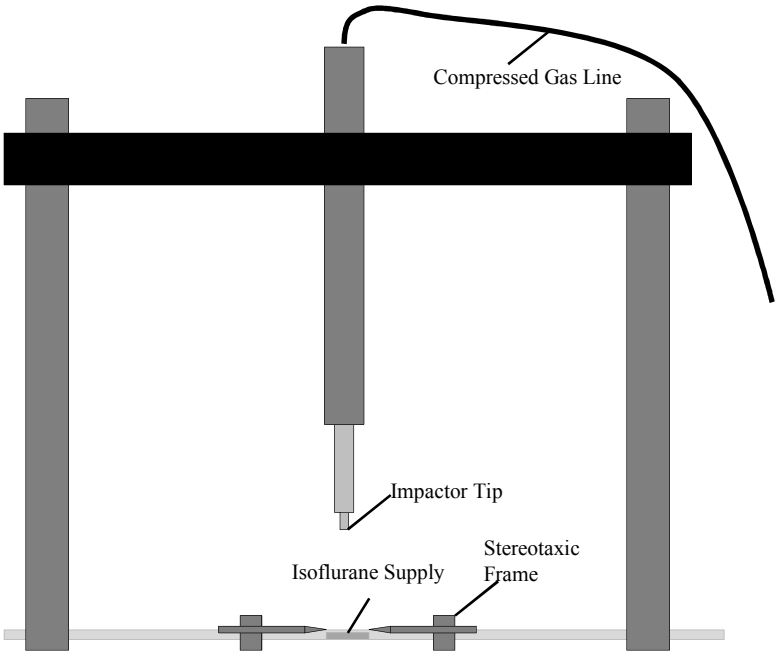

Figure 17 Representation of the CCI impactor used to induce controlled TBI. Used with minor modifications from **[1-3].**

shaft is then returned to the fully retracted position, and the crosshead is lowered to the desired level of compression. The impact velocity can be controlled using compressed gas pressure from 1-7 m/s [1-3].

Table 5 Genes that regulate necroptosis (Adapted from [114]).

Symbol	Name
Tmem57	transmembrane protein 57
Grb2	growth factor receptor bound protein 2
Pvr	poliovirus receptor
Foxi1	forkhead box l1
Jph3	Juntophilin 3
Rab25	RAB25, member RAS oncogene family
S100a7a	8100 calcium binding protain A7A
4933439F11Rik	RIKEN cDNA 4933439F11 gene
4732429D16Rik	RIKEN cDNA 4732429D16 gene
9430015G10Rik	RIKEN cDNA 9430015G10 gene
Bmf	Bcl2 modifying factor
Defb1	defensin beta 1
Eif5b	Eukaryotic translation initiation factor 5B
Dpysl4	Dihydropyrimidinase-like 4
Commd4	COMM domain containing 4
Txnl4b	Thioredoxin-like 4B
F730015K02Rik	RIKEN cDNA F730015K02 gene
Hspbap1	Hspb associated protein 1
Mag	Myelin-associated glycoprotein
Mrcl	mannose receptor-like precursor
Hoxa3	Homeo box A3
Kcnip1	Kv channel-interacting protein 1
Galnt5	UDP-N-acetyl-alpha-D-galactosamine: polypeptide N-acetylgalactosaminyl1transferase 5
Olfr1404	Olfactory receptor 1404
Parp2	poly (ADP-ribose) polymerase family member 2
Tnfrsf1a	Tumor necrosis factor receptor superfamily, member 1a
Sycp2	synaptomenal complex protein 2
Atp6v1g2	ATPase, H+ transporting, lysosomal V1 subunit G2
Nudt13	nudix (nucleoside diphosphate linked moiety X)- type motif 13
Spata2	spermatogenesis associated 2
cyld	Cylindromatosis 1
Tnfaip8l1	tumor necrosis factor, alpha-induced protein 8-like 1

The goals of this study are to adapt previous studies using necrostatins to work with a functional, therapeutic TBI model, achieve localized delivery of necrostatins to the injury site, and to maintain controlled release over time as the film degrades. This study proposes to use drug delivery of various necrostatins from silk fibroin films as a method to prevent necroptosis following CCI. Necroptosis is defined as a regulated cellular necrosis mechanism, independent from apoptosis [114, 115]. More specifically, necroptosis is a mechanism of necrotic cell death induced by apoptotic stimuli in the form of activation of the death domain receptor by their respective ligands while apoptosis is inhibited [115]. There are 25 genes that have been

identified as required for necroptosis when induced by zVAD.fmk and TNFα, but not for apoptosis [**Table 5**]. The goal of this study is to delivery necrostatins from silk films to the CCI injury site in order to inhibit necroptosis, and minimize tissue damage. Necrostatins have been proven to inhibit non-apoptotic cell death, which is an important contributor to pathological cell damage in mouse models of cerebral ischemia and myocardial infarction [116, 117]. It is believed that necrostatins inhibit necroptosis through inhibiting RIP1 kinase activity [115, 116].

Although drug delivery from silk fibroin substrates has been very well documented [18-20, 26, 30, 35, 36, 39, 118-121], an *in vivo* application for drug delivery for a TBI CCI mouse model has yet to be done with any form of localized drug delivery. Necrostatin-1 (Nec-1) [122-127] and Necrostatin-3 (Nec-3) [128, 129] are anti-necroptotic signaling factors that have been extensively studied for their roles in preventing necroptosis through inhibition of RIP1 kinase activity. Silk fibroin films were loaded with Nec-1 or Nec-3 and implanted *in vivo* in conjunction with a CCI mouse model to study the effect on CCI-induced necroptosis. Silk films were also loaded with propidium iodide (PI) as a marker of apoptosis or necrosis [130-134].

B. Materials & Methods

1. Silk Film Preparation

Silk solution was prepared from *Bombyx mori* cocoons as outlined in the previous chapters. The purified silk solution was diluted to 2% (w/v), and the drug(s) of choice were mixed in gently by inversion. A Polydimethylsiloxane (PDMS) mold was cast with raised 5mm-diameter cylinders in an 8 x 12 pattern [Figure 2]. 13μL of the EB / silk solution was pipetted onto each raised cylinder and spread with a pipette tip to cover the entire surface of the cylinder. Films were rendered water insoluble by introduction of

β-sheets through water-annealing in a vacuum for 3 hours in the presence of a water source at room temperature [103-105]. After water annealing, films dried and carefully lifted from the PDMS mold using a scalpel and forceps. The films were stored at room temperature and protected from light.

2. *In vitro* Release

Prior to any *in vivo* studies, *in vitro* release profiles were gathered for controlled release of FITC-Dextrans (3-5 kDa and 70kDa) and EB. Films were loaded with 10 $^{mg}/_{mL}$ of EB or FITC-Dextrans and once cast and water-annealed, were placed in a 96-well plate with 200μL PBS in each well. The films were transferred to a fresh PBS well at each time point, and the wells were read using a UV-Vis plate reader. Absorbance for EB was read at 620nm, and fluorescence for FITC-Dextrans was read at Excitation 490nm, Emission 525nm.

3. *In vivo* Release

For *in vivo* studies, Evans blue (Sigma), propidium iodide (PI) (Sigma), Necrostatin 3-FITC, and Necrostatin-1 (both donated by collaborators) were loaded into silk films in the following concentrations: EB (4 μg/film), PI (1 μg/film or 3.75 nmol/film), Necrostatin-1 and -3-FITC (8 μmol/film), and. The number of animals used in each study is as follows: EB (n = 6), PI (n = 12), necrostatin-3 (n = 3), necrostatin-1 (n = 5), vehicle film (n = 5 for PI, n = 5 for necrostatin-1). These films

Table 6 Experimental setup for each animal trial. Control (Ctrl) conditions did not contain any necrostatins. Blank Ctrl films were empty silk films that contained no drugs/stains.

Condition	Drus/Stain	Concentration	Number of Animals
1	EB	4 μg	6
2	PI	1 μg	12
3	Hoechst PI	2 μmol 1 μg	3
4	Nec-3-FITC	8 μmol	3
5	Nec-1	8 μmol	5
2 (Ctrl)	Blank	N/A	5
5 (Ctrl)	Blank	N/A	5

were delivered in conjunction with a CCI mouse model performed at MGH Neuroscience Center. Films were implanted after the craniectomy, but either before or after the CCI to examine the effects of necrostatins on cell injury.

4. CCI Model

For the mouse CCI model, a CCI device similar to Figure 17 was used. The implantation and trauma protocol (2004N000286) were approved by the Massachusetts General Hospital Institutional Animal Care and Use Committee and comply with the NIH Guide for the Care and Use of Laboratory Animals.

. Mice (CL7/BL6, 3 months of age, Jackson Laboratories, Bar Harbor, ME) were anesthetized with 4% isoflurane, 70% N_2O and O_2 and positioned in a stereotaxic frame. Isoflurane delivery was maintained via an opening in the tubing leading from the anesthesia box and isoflurane was titrated to quiet respirations and ensure a lack of toe-pinch response [110]. A 5-mm craniotomy was made using a surgical hole saw over the left parietotemporal cortex (the center of the coordinates of craniotomy relative to bregma: 1.5 mm posterior, 2.5 mm lateral).

CCI was produced using the previously mentioned CCI device with a velocity of 6 m/s, and an impact depth of 0.3 mm. Sham injury involved craniotomy but no cortical impact. The silk film was placed directly on top of the cortex prior to the CCI. The craniotomy was then replaced and the scalp was sutured. Mice were returned to their cages to recover from anesthesia and left for 14 days. For implants of drug films and control vehicle films, the dura mater remained intact.

5. Immunostaining

For sacrificing, the mice were deeply anesthetized with isoflurane and decapitated. The brains were removed and frozen using liquid nitrogen vapor by floating

them in a weigh boat over liquid nitrogen. Coronal sections (14 μm) were collected (200-250 μm apart) from the anterior to the posterior brain, mounted on poly-L-lysine-coated slides and stored at -80°C. Fluorescence images were acquired on a Leica DM IL fluorescence microscope with excitation at 540 nm and emission at 680 nm. Using fluorescence microscopy, propidium iodide-positive cells were counted in a total of three brain sections located within the center of the contusion (bregma -1.90 to -2.70) and separated by at least 250 μm, for a total of 9 cortical fields assessed per animal. Cell count data for each mouse were the average of the nice cortical brain fields.

C. Results & Discussion

1. *In vitro* Release

For *in vitro* release studies, controlled release was achieved from silk films that contained 3-5 kDa and 70 kDa FITC-Dextrans and EB [Figure 19]. While the burst release occurred over the first few hours [Figure 19], as the films degrade *in vivo* as shown by [15, 40, 41], the remaining FITC-Dextrans or EB would be released slowly over time. The increased release of the 3-5 kDa FITC-Dextran over the 70 kDa FITC-Dextran is expected due to the smaller size of the molecule which allows for it to diffuse out of the film more quickly once the film has swollen after being rehydrated. The lower release rate of the EB from the films, however, may be due to the EB sticking to the silk.

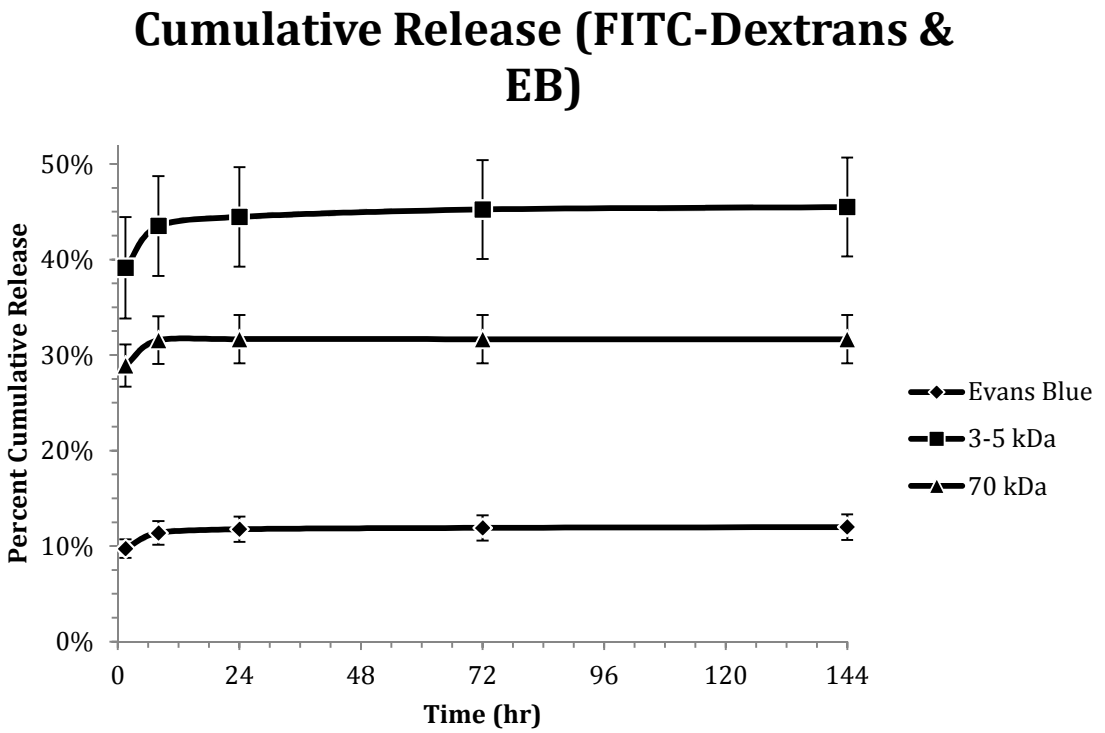

Figure 19 Controlled release of 3-5 kDa and 70 kDa FITC-Dextrans and EB was achieved over 6 days. Silk films were placed in 200µL PBS in a 96-well plate. Films were transferred to new wells containing fresh PBS at each time point. Release was quantified using a UV-Vis plate reader using Absorbance for EB at 620nm and Fluorescence for FITC-Dextrans at Excitation 490nm and Emission 525nm. Error bars represent standard deviation, n=6 for all groups.

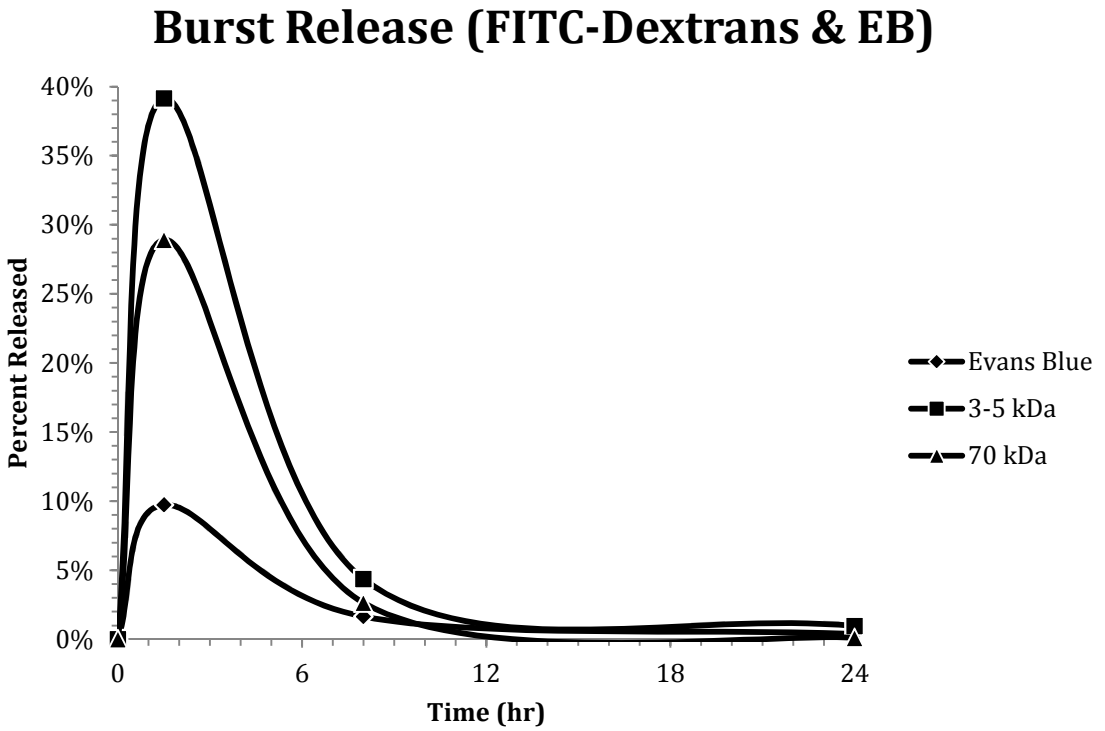

Figure 19 Burst release of 3-5 kDa and 70 kDa FITC-Dextrans and EB. Silk films were placed in 200µL PBS in a 96-well plate. Films were transferred to new wells containing fresh PBS at each time point. Release was quantified using a UV-Vis plate reader using Absorbance for EB at 620nm and Fluorescence for FITC-Dextrans at Excitation 490nm and Emission 525nm. Error bars represent standard deviation, n=6 for all groups.

2. *In vivo* Release

Controlled release of EB was achieved over 8 days *in vivo* [Figure 20] using the same silk films used for *in vitro* release. The films exhibited sustained release over 8 days in which EB was seen to diffuse through the dura mater and into the cortex, ultimately reaching the ipsilateral hippocampus CA3 region. EB diffusion rate through the cortex was calculated over the same time period [Figure 23] using Image J (NIH). This demonstrated the ability of silk films to effectively deliver drugs thorugh the dura mater into the cortex of mice.

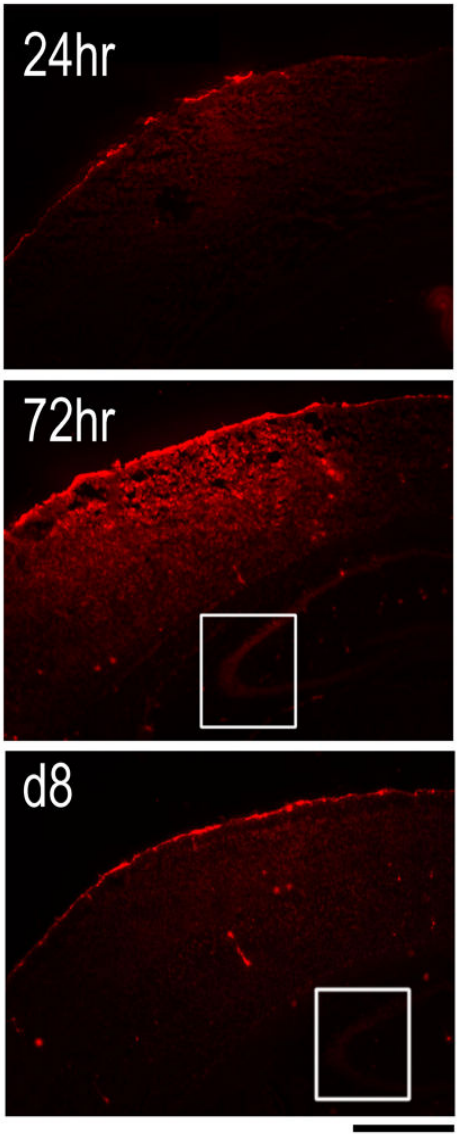

Figure 20 EB diffusion (red) through coronal sections of the cortex at 24, 72 and 192 hr post-implantation. Ipsilateral hippocampus CA3 regios denoted by white box. Scale bar 500µm. Reproduced with permission from Dr. Min Tang-Schomer.

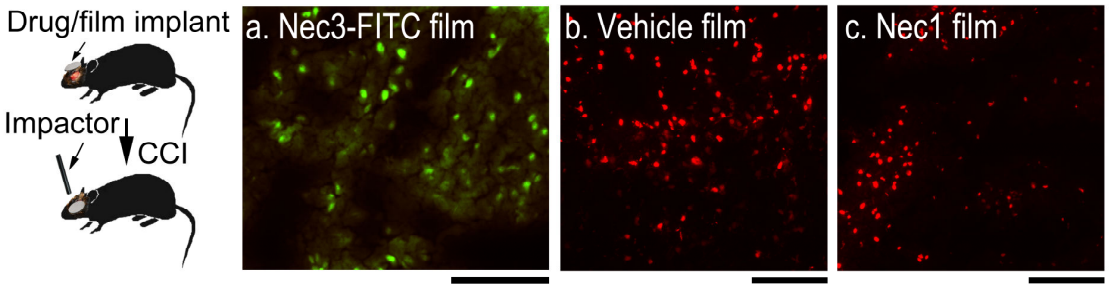

Figure 21 Fluorescence images of silk films delivered to the cortex before CCI. (a.) Nec-3-FITC was loaded into silk films and shows successful uptake by damaged neurons (green). (b.) Vehicle control films were placed on the cortex, but contained no therapeutic drugs and displayed increased cell injury post-CCI. (c.) Nec-1 films exhibited decreased cell injury post-CCI as compared to the vehicle control films. For (b.) & (c.) injections of PI (250 µg/ml in PBS) were administered 5 hr post-CCI to stain injured cortical cells. PI positive cells marked in red (b.) & (c.). Scale bar = 100µm. Reproduced with permission from Dr. Min Tang-Schomer.

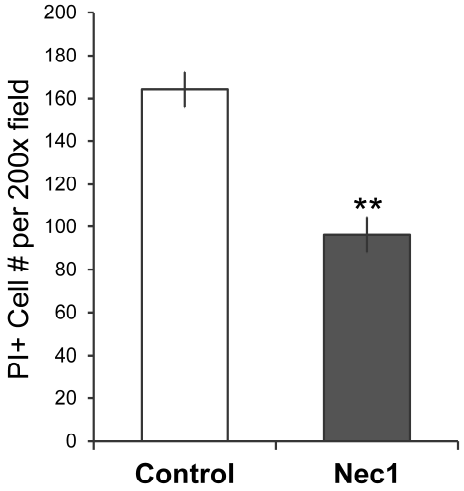

Figure 22 Quantification of PI positive cells (injured cells) in CCI injured brains. Control counts (vehicle control films) contained significantly higher injured cell counts than Nec-1 film counts.** signifies $0.001 < p < 0.01$. Reproduced with permission from Dr. Min Tang-Schomer.

promising results, the ability of silk films to deliver therapeutic drugs in a disease model was explored.

Nec-1 and Nec-3-FITC were loaded into silk films and delivered to the cortex of mice *in vivo* prior to a CCI, and the EB appears to have been cleared *in vivo* over time (less fluorescence on day 8 vs. day 3) but the continuing fluorescence indicated the continued release of EB from the films over an extended period of time. Film degradation was not examined over this time period, but it is possible that the extended EB release may have been due to film degradation *in vivo* leading to prolonged EB release. Using this data and the

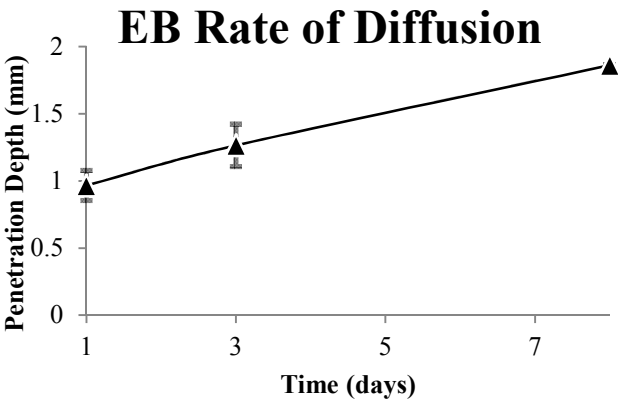

Figure 23 EB diffusion through the cortex over 8 days. Measured as the center distance of its radial diffusion profile using Image J (NIH). Error bars indicate standard deviation

subsequent cell damage was examined [Figure 21]. Fluorescence microscopy images of coronal plane sections of cortical brain tissue indicated significantly higher cell injury post-CCI for the vehicle control films (no necrostatins) as compared to therapeutic films (Nec-1 or Nec-3-FITC) [Figure 22]. Cell counts of PI positive cells (red) in cortical sections with vehicle control films were significantly higher ($p < 0.01$) than those for the cortical sections which received Nec-1 films. This data demonstrates successful reduction of necroptosis *in vivo* using localized necrostatin drug delivery in a therapeutic mouse disease model.

D. Conclusions

Silk fibroin films have illustrated an excellent ability to deliver and stabilize various drugs and dyes, as well as stabilize vaccines [21]. With the results of this study, is has been illustrated that silk fibroin films have the ability to deliver therapeutic drugs *in vivo* in an animal disease model of TBI, and also to maintain controlled release of these therapeutic agents over time as the films degrade. Future possible directions for this technology could be for chemotherapeutic treatment of an animal meningioma model in which the films are laid on top of the dura mater to help treat tumors in the meninges. This new application of silk films also has potential in other disease models such as treating epilepsy that might be located towards the surface of the cortex.

Chapter 4. Silk Fibroin films as vehicles for controlled gene delivery using adeno-associated viral vectors

A. Introduction

Adenoassociated viral vectors (AAVs) are exceptionally effective tools for gene delivery, having up to 12 serotypes, and are part of the *parvoviridae* family and Dependovirus genus. Members of the Dependovirus genus require a helper virus such as a regular adenovirus or herpes simplex virus to facilitate infection and replication. In the absence of a helper virus, AAVs establish a latent infection within the cell. This is beneficial because it ensures long-term, stable expression of the vector gene. The virion shell is approximately 25 nm in diameter and encapsulates a single-stranded DNA genome of 4.7 kb [135].

The main attractions of AAVs over lentiviruses and other retroviruses are their high titer production capabilities, lack of pathogenicity, long-term transgene expression and wide range of targets. AAVs have been used to target numerous different organ types including bone [136, 137], bone marrow [138, 139], cardiac muscle [140-142], liver [143-146], kidney [147-149], lung [150-152], retina [153-156], skeletal muscle [157-161], central

Table 7 Targeted organs (and diseases) and their respective AAV serotypes. rAAV indicates recombinant AAV.

Tissue	Serotypes	References
Bone	rAAV	[136, 137]
Bone marrow	2, 5	[138, 139]
Cardiac muscle	2, 8-9	[140-142]
Liver	8-9	[143-146]
Kidney	1-5	[147-149]
Lung	1-9	[150-152]
Retina	2, 4-5	[153-156]
Skeletal muscle	1, 6-9	[157-161]
CNS	1-2, 4-5, 8-10	[162-176]
Huntington's		[164-166]
Parkinson's		[163, 173]
Alzheimer's		[172, 174-176]
Glioma		[167-169]
Schwannoma		[162]
Pancreas	8	[29, 177]
Vascular tissue	1-2, 9	[178-180]

nervous system (CNS) [162-176], pancreas [29, 177] and vascular tissue [178-180].

This study will used AAV8 and AAV9 due to their high efficacy at transducing neural cells. AAV8 and AAV9 have been used in recent years for numerous different CNS disease models such as Huntington's disease [164-166], Parkinson's disease [163, 173], Alzheimer's disease [172, 174-176], glioma [167-169], and schwannoma [162].

Current models for CNS disease models typically involve stereotaxic injection of AAV into the region of interest. While controlled release mechanisms of gene delivery have been achieved using this method, controlled release method of delivering AAVs that does not damage cortical tissue has yet to be achieved. The benefit of such a system would be to use current AAV models are becoming increasingly efficient, and limit their release to the region of interest without causing any damage to the cortex. Using silk fibroin films, localized transduction of dural fibroblasts as well as local subdural neurons can be achieved. Silk films are also an ideal delivery vehicle for mengioma due to the localization of the release to the surface of the dura mater. Stereotaxic injections would be extremely difficult to perform for this particular model, and therefore silk films present an extremely exciting new alternative delivery method.

Silk fibroin biomaterial systems have been explored extensively as delivery vehicles for drugs [18, 20, 35, 37, 38, 118, 121] and genes [120, 181, 182], as well as for the stability of drugs [18, 20, 35, 37, 38, 118, 121] and vaccines [21], but direct delivery of viral vectors has yet to be achieved using silk films. The goals of this study were to:

1. Establish controlled release of viral vectors over time
2. Maintain sustained delivery over time as the films degrade
3. Demonstrate *in vivo* transduction

AAV8-GFP and AAV9-GFP serotypes were chosen for transduction of dural fibroblast and subdural-neurons due to their ability to successfully permeate the blood brain barrier (BBB) [183-187].

B. Materials & Methods

1. Silk Film Preparation

Silk solution was prepared from *Bombyx mori* cocoons which were boiled for 45m in a 0.02M sodium carbonate solution, rinsed three times with distilled water and dried overnight. The extracted silk fibroin was then dissolved in a 9.3M LiBr solution at 60°C for 4 hours. The solution was then dialyzed in distilled water using Slide-a-Lyzer dialysis cassettes (MWCO 3500, Pierce) for 2 days to remove the LiBr from the solution.

After purification of the silk solution, AAV9-GFP ($3.5 \times 10^{10\text{-}12\ g.c.}/_{mL}$) was loaded into the silk solution such that it would yield a concentration of $2.33 \times 10^{8\ g.c.}/_{mL}$ or $3.85 \times 10^{10\ g.c.}/_{mL}$ per film and a 2% (w/v) silk concentration. Silk-AAV9 films were cast on a PDMS mold with 4mm-diameter raised cylinders [Figure 2]. 13µL of Silk-AAV9 solution was added to each raised cylinder and spread out using a pipette tip to cover the entire surface of the cylinder. The films were then left in a tissue culture hood to dry at room temperature. Once dry, the films were water annealed in a vacuum chamber for 45 minutes to induce β-sheet formation, and then left to dry again in a tissue culture hood. Once dry, the films were carefully lifted off the surface of the PDMS cylinders with a #10 scalpel and forceps, being very careful to avoid cracking the film by keeping the angle of incidence of the scalpel blade as high as possible. Films were stored in Parafilm-wrapped tissue culture petri dishes at 4°C until use.

2. AAV Preparation

AAVs were produced by transfection of human 293T cells with AAV and helper DNA plasmids using the calcium phosphate technique. Seventy-two hours post-transfection cells were harvested and the virus was purified from crude cell lysates by iodixanol gradient centrifugation followed by de-salting and concentration using Millipore Amicon Ultra centrifugal devices (Billerica, MA). The vector titer (in genome copies/ml [$^{g.c.}/_{mL}$]) was determined using a quantitative TaqMan PCR assay using TaqMan® Fast Universal PCR Master Mix (Applied Biosystems, Foster City, CA), a TaqMan probe (6FAM-TGCCAGCCATCTGTTGTTTGCC—MGB, Applied Biosystems) and primer set (Forward primer, CCTCGACTGTGCCTTCTAG ; Reverse Primer, TGCGATGCAATTTCCTCAT), which specifically binds to a conserved region of the poly A region of the transgene cassette. A standard curve was prepared using serial dilutions of an AAV-GFP plasmid of known molar concentration. The quantitative PCR was performed in an Applied Biosystems 7500 Thermal cycler using the following conditions: 1 cycle, 94°C 30 s; 40 cycles, 94°C 3 s, 60°C 30 s.

3. *In vitro* Release

Virus release was characterized *in vitro* before proceeding to *in vivo* studies. The swelling of the films was first characterized by examining the swelling behavior of 45m boil-time silk films water annealed for 30m, 45m and 60m. Films were then placed into 48-well plate filled with 500µL of distilled water and observed intermittently for up to 48 hours. Using the results from the film swelling characterization studies, the 45m boil-time, 45m water-annealed films were chosen as the ideal candidates for AAV9 release characterization. These films were loaded with 7 x $10^{7\text{-}8\ g.c.}/_{mL}$ AAV9-GFP and AAV8-GFP and placed in a 24-well plate 1µm pore size transwell system [Figure 24]. The films

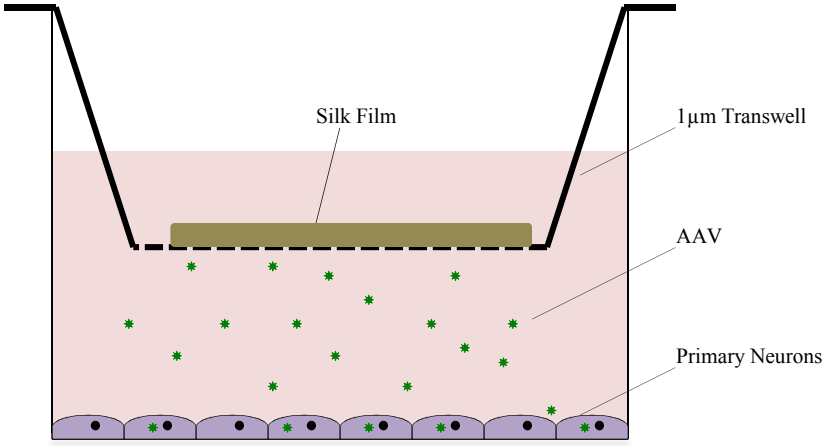

Figure 24 Silk film delivery vehicle in a transwell system for AAV release on to cultured primary neurons

were placed in the transwell, and the well of the plate was filled with 500µL Neurobasal medium. The medium was collected at different timepoints and replaced with fresh medium.

For *in* vitro release on to cells, cortical neurons were plated in the same 24-well plates underneath the transwell system. At various time points, the cells were immunostained for βIIITB, MAP2 and GFAP. The amount of AAV9-GFP and AAV8-GFP released was quantified using qPCR (as outlined in AAV preparation protocol).

4. *In vivo* Release

For implantation, mice were anesthetized with isoflurane, an incision was made through the scalp and a 4mm-diameter craniotomy was performed using a 4mm-diameter bone hole saw [63]. Depending on the experimental conditions, a durotomy was also performed in the area of the craniotomy. The Silk-AAV9 film was then placed directly onto the surface of the dura or brain if a durotomy was performed. The craniotomy bone flap was then replaced and the scalp incision was sutured.

After 14 days, the mice were anesthetized with an IP injection of ketamine and an intracardiac perfusion with formalin was performed to fix the tissues, followed by decapitation to collect the brain. The brains were then placed in sucrose. Following sucrose perfusion, the brains were frozen with isopentane and dry CO_2 and stored in -

80°C until being sectioned. Brains were sectioned in 14µm sections approximately 240µm segments (14µm sections x 8, skip ahead 9 sections).

The implantation protocol (2004N000286) was approved by the Massachusetts General Hospital Institutional Animal Care and Use Committee and comply with the NIH Guide for the Care and Use of Laboratory Animals.

5. *In vivo* Experimental Setup

The first *in vivo* experiment contained regular Silk-AAV9 films (loaded with 2.33 x $10^{8\ g.c.}/_{mL}$ AAV9) as well as Silk-AAV9 films with DMSO that was theorized to aid in dura mater permeability. The experimental setup is shown in Table 8.

For the second *in vivo* experiment, the DMSO was not included in the films and no duratomies were performed. The goal of this trial was to see if the AAV9-loaded films could transduce dural fibroblasts. The concentration of AAV9 was increased to 3.85 x $10^{10\ g.c.}/_{mL}$. Films were implanted into 3 adult mice and 1 immature mouse [Table 9].

Due to a miscommunication between collaborators, the brains were accidentally frozen before being placed in sucrose and the sections were not suitable for immunostaining. Therefore this trial was restarted under the same conditions but with only 3 adult mice and no immature mice.

Table 8 Experimental design for *in vivo* trial. Stereotaxic injections contained 2.33 x $10^{8\ g.c.}/_{injection}$ at a flow rate of 0.2 $^{\mu L}/_{min}$ for 5 min (into striatum). The sham control mouse had a craniectomy and duratomy, but no film was implanted.

Mouse	Condition	DMSO	Duratomy	Hemisphere (Coordinates)
1	AAV9 Silk Film	Yes	No	Left
2	AAV9 Silk Film	Yes	No	Left
3	AAV9 Silk Film	Yes	Yes	Left
4	AAV9 Silk Film	No	Yes	Right
5	AAV9 Silk Film	No	Yes	Right
6	AAV9 Silk Film	No	No	Right
7	Stereotaxic Injection	No	No	Right (x=-2.0 y=0.5 z=-0.2)
8	Stereotaxic Injection	No	No	Right (x=-2.0 y=0.5 z=-0.2)
9	Sham	No	Yes	Right

Table 9 Experimental design for *in vivo* trial with increased AAV9 loading concentration. DMSO was not added to the films and no duratomies were performed.

Mouse	Condition	Age
1	AAV9 Silk Film	Adult
2	AAV9 Silk Film	Adult
3	AAV9 Silk Film	Adult
4	AAV9 Silk Film	Immature

C. Results & Discussion

1. *In vitro* AAV Delivery

The first *in vitro* films were made of 45m boil-time silk and water annealed for 60m. The films were released through the transwell system over cultured primary neurons to examine transduction efficiency *in vitro.* The results from this study were that the films were very water insoluble and therefore released only 0.002% of the initial loading concentration [Figure 26]. The cultured neurons were examined under fluorescence microscopy [Figure 26]. Fluorescence microscopy illustrated successful transduction of cultured cortical neurons *in vitro*. Transduction efficiency was quantified by comparing the transduction from a silk film to the same amount of vector delivered in solution directly to the culture medium. The transduction from the films was approximately 56% that of the transduction from a vector solution, suggesting that the films released approximately 56% of the viral titer.

After this study, in order to explore the water solubility of the films, the same films were water annealed for 30m and the release kinetics were observed. It was also postulated that aggregation of the viral particles prior to encapsulation in the silk films might be a limiting factor in the release from the films. Sodium citrate was added to the films to yield a concentration of 510mM in the silk solution, which was reported to yield 96% recovery of AAV particles without aggregation [188]. The results were that the films resolubilized almost immediately when placed in Neurobasal medium. As a result, the vast bulk of the virus was released in the first day. The effect of the sodium citrate in

the films was negligible, and is likely due to the fact that any AAV particle aggregation took place during FPLC purification and the sodium citrate was unlikely to reverse the

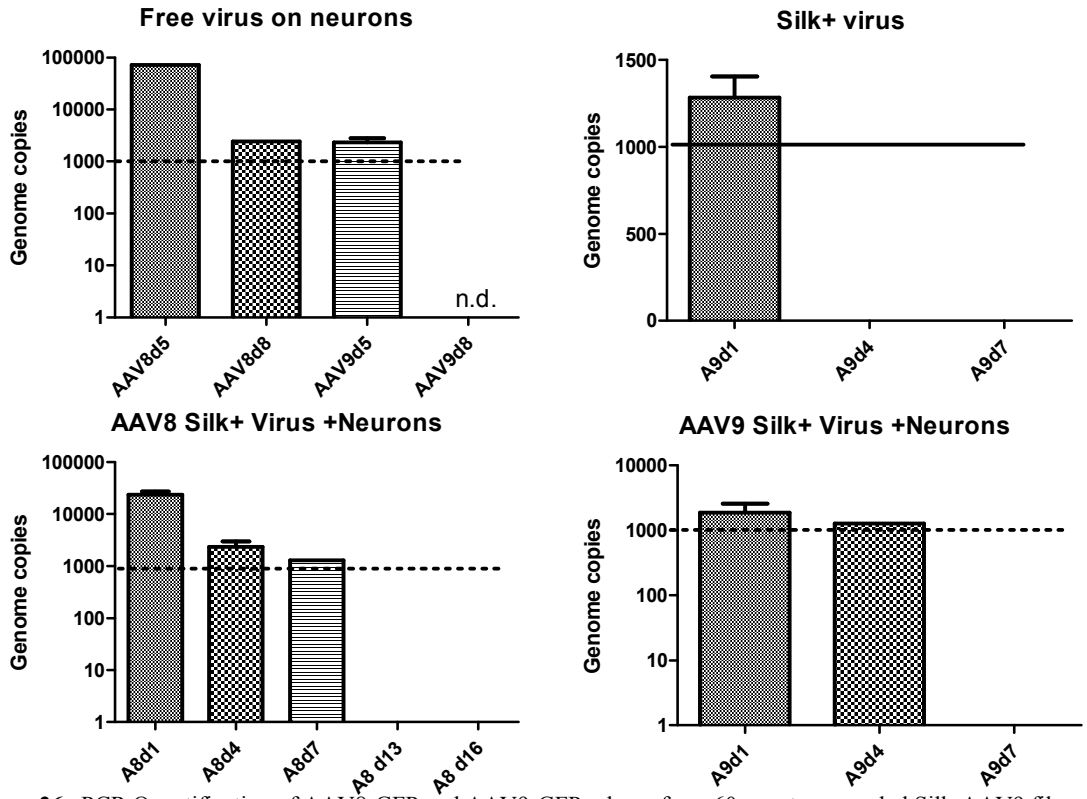

Figure 26 qPCR Quantification of AAV8-GFP and AAV9-GFP release from 60m water-annealed Silk-AAV9 films (7 x 10^{7} $^{g.c.}/_{mL}$). Silk-AAV9 films were released through transwell system over cultured primary neurons, but these images proved inconclusive and it was decided to analyze *in vivo* transduction instead (under the assumption that AAV9 transduction didn't work very well in an *in vitro* model).

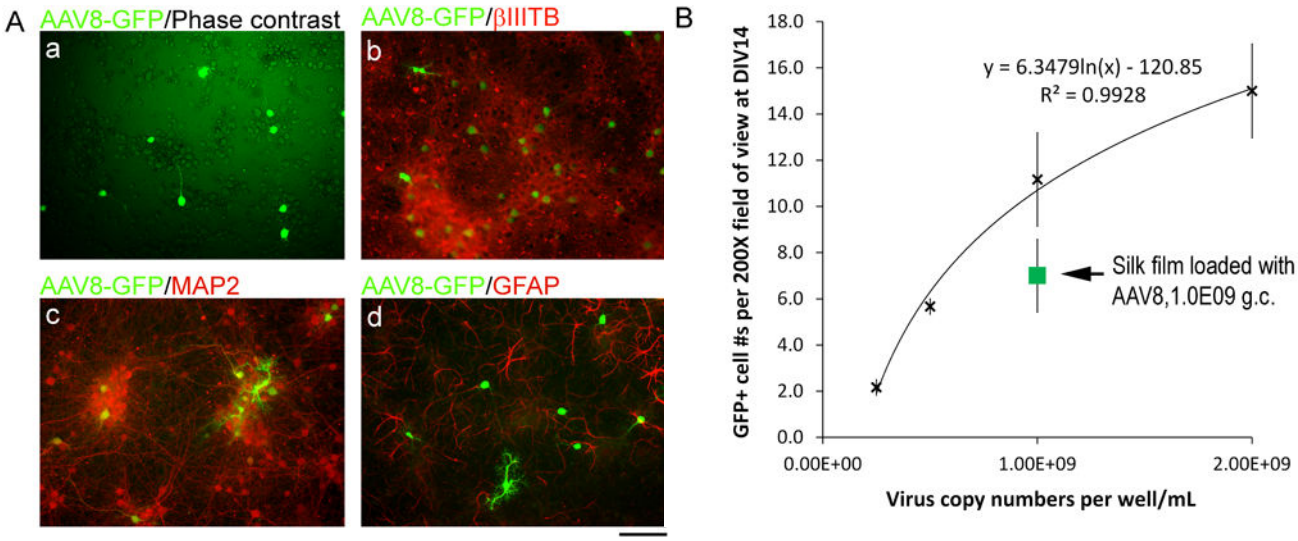

Figure 26 (A) Fluorescence microscopy images of cortical neuron transduction from AAV8-GFP silk films using the transwell delivery system. (a) Phase contrast images of cortical neurons expressing GFP. (b) Immunostaining with neural cytoskeletal marker βIIITB, (c) MAP2, and (d) astrocyte marker GFAP. (B) Quantification of AAV8-GFP transduction following release from silk films (1 x 10^{9} g.c./mL, green) compared with AAV8-GFP delivered as a solution. Suggests ~56% AAV8-GFP successfully released from films in culture. Scale bar = 100µm. DIV = days *in vitro*. Reproduced with permission from Dr. Casey Maguire & Dr. Min Tang-Schomer.

aggregation. Instead the sodium citrate should likely have been added to the buffer during FPLC purification.

Next, the film swelling was characterized. It was postulated that the key to the controlled release of the AAV particles might lie in the swelling behavior of the films once placed in an aqueous solution. 30m, 45m and 60m water-annealed silk solution films were prepared and the swelling in distilled water was observed over 48 hours at 37°C. It was observed that the 30m water-annealed films resolubilized almost immediately, which is representative of the results seen in the second *in vitro* release study. The 45m water-annealed films swelled approximately 2-2.5x their original surface area from 5mm in diameter to 7-8mm in diameter. Once swelled, these films remained in this configuration over 48 hours of incubation at 37°C and did not resolubilize. The 60m water-annealed films did not swell at all.

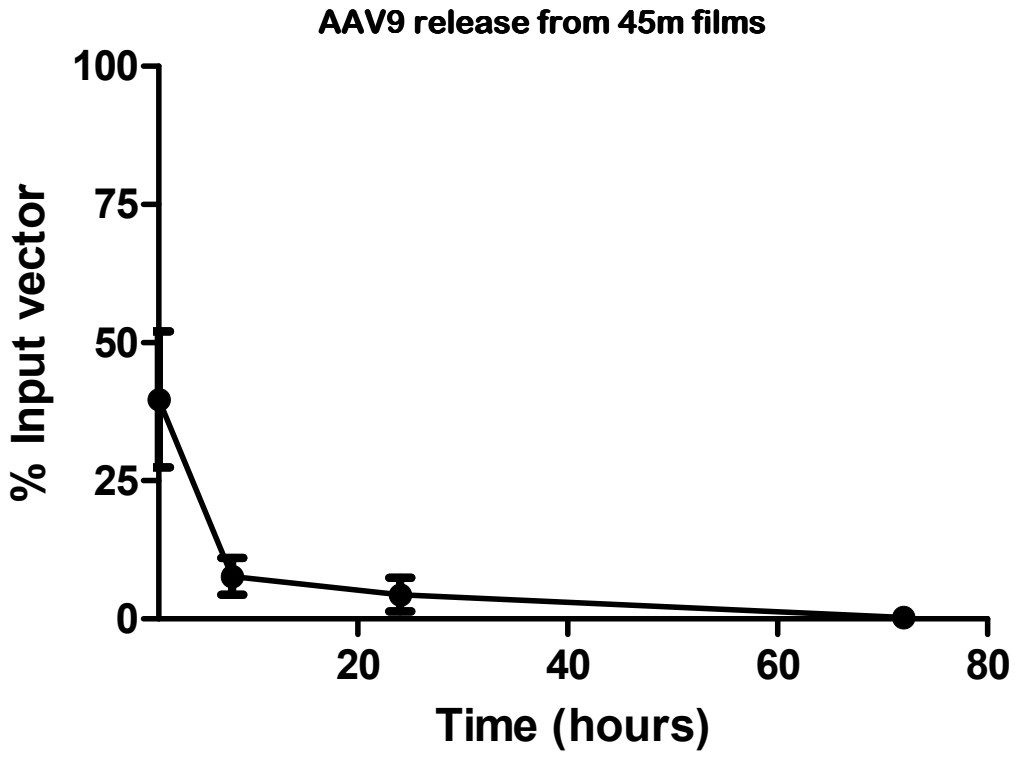

Figure 27 AAV9-GFP release kinetics for 45m boil-time Silk-AAV9 films water annealed for 45m.

Given these results, the 45m water-annealed films were chosen as candidates for further *in vitro* studies. The AAV9-GFP loading concentration was increased to 7 x 10^8 $^{g.c.}/_{mL}$ to increase transduction efficiency *in vivo*. After this study, the results were much more promising and showed controlled release of approximately 55% of the initial loading concentration steadily over the first 24 hours [Figure 27]. It is assumed that as the film degraded *in vivo* the remaining virus would be slowly released as well. It was also postulated that these films would degrade better than the 60m water-annealed films *in vivo* due to their swelling characteristics.

2. *In vivo* AAV Delivery

Following the results of the *in vitro* characterization, the 45m boil-time and 45m water-annealed films were chosen for the *in vivo* model. For the first *in vivo* model, the

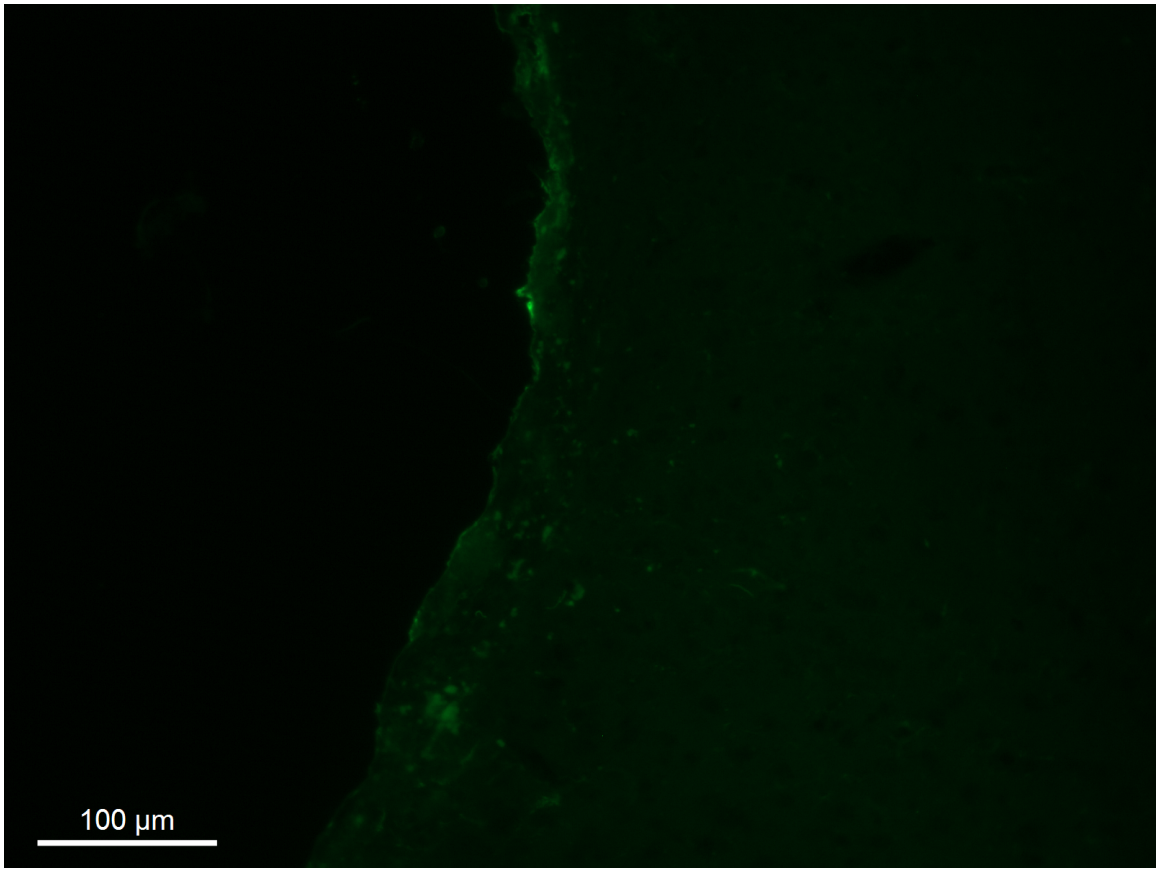

Figure 28 Fluorescence microscopy images (From Tufts microscope) showing both native GFP fluorescence and also Anti-Vimentin staining. Silk film with AAV9 and DMSO with dura intact.

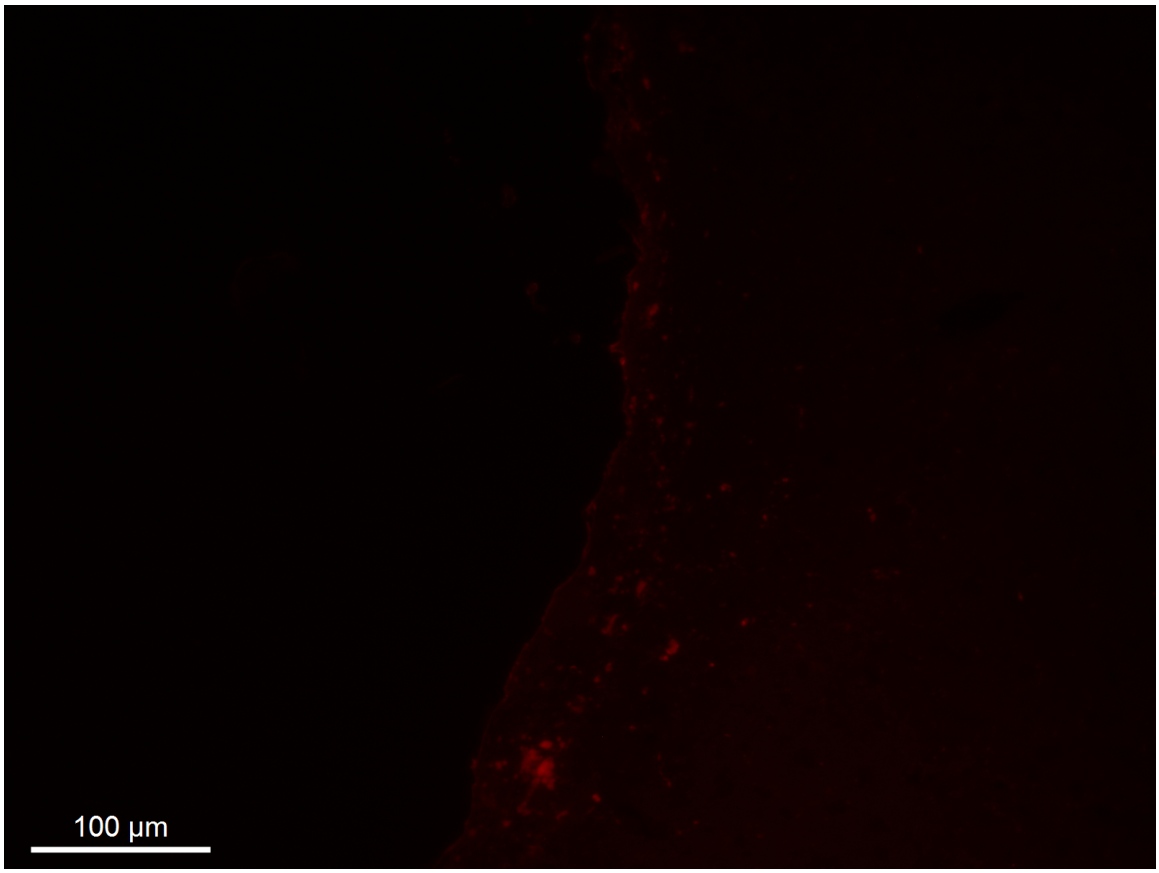

Figure 29 Fluorescence microscopy images (From Tufts microscope) showing Anti-GFP staining with Alexa Fluor® 594. Silk film with AAV9 and DMSO with dura intact.

sections were stained first with Rabbit Anti-Vimentin, followed by Goat Anti-Rabbit Alexa Fluor® 488. Following this, they were stained with Rabbit Anti-GFP conjugated with Alexa Fluor® 594 [Figure 28Figure 29 (Both from same section under different optical filters)]. This was a lapse in judgement in that by staining with the Alexa 488 secondary for the Vimentin, it overlapped with the native GFP fluorescence. It was decided that it was necessary to increase the loading concentration for the following trial regardless of this error, so the second animal experiment was undertaken with a higher loading concentration.

For this second trial, the viral concentration was increased and films were implanted into 3 mice. After 14 days, the animals were sacrificed and the sections were

stained for GFP, NeuN, and DAPI [Figure 30]. GFP (green), NeuN (red) and DAPI (blue) fluorescence can clearly be seen in these images. GFP fluorescence is localized to the dura mater, however, suggesting that the AAV9 vectors transduced the dura mater almost exclusively. This data is extremely promising for future disease models such as meningioma since it would allow for localized transduction of the meninges. Future studies will attempt to further increase the viral concentration, and to focus on a meningioma model. Further *in vitro* characterization will also be pursued.

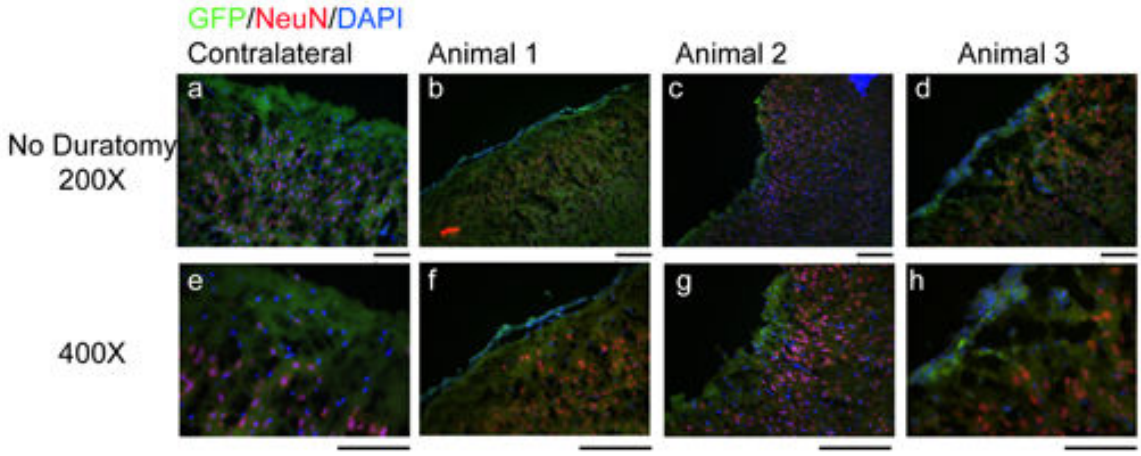

Figure 30 Immunostaining of cortical sections illustrating dural transduction using AAV9-loaded (3.85×10^{10} g.c./film) silk films. No duratomy performed prior to film implantation. Scale bar = 100µm. Reproduced with permission from Dr. Min Tang-Schomer.

D. Conclusions

It was shown *in vitro* that silk films are capable of controlled gene delivery over time, and that as the films degrade over time, they would slowly continue to release the loaded viral vectors. In addition, *in vivo* gene delivery was also demonstrated successfully. The silk films were also able to keep transduction localized to the region immediately surrounding the implantation site. The results of these gene delivery studies are extremely promising for future animal models. While mostly exploratory, these studies have paved the way for a future meningioma model using AAV8 or AAV9 or a combination of both. Transduction can be targeted to sub-dural cortical tissue or to the

dura mater itself depending of the dura mater is left intact prior to implantation. Similarly to with the controlled drug delivery study, there are numerous potential future applications for these films in genetic neurological diseases such as Alzheimer's, Huntington's and Parkinson's.

References

1. Lighthall, J.W., *Controlled cortical impact: a new experimental brain injury model.* Journal of neurotrauma, 1988. **5**(1): p. 1-15.
2. Lighthall, J.W., H.G. Goshgarian, and C.R. Pinderski, *Characterization of axonal injury produced by controlled cortical impact.* Journal of neurotrauma, 1990. **7**(2): p. 65-76.
3. Edward Dixon, C., G.L. Clifton, J.W. Lighthall, A.A. Yaghmai, and R.L. Hayes, *A controlled cortical impact model of traumatic brain injury in the rat.* Journal of neuroscience methods, 1991. **39**(3): p. 253-262.
4. Leisk, G.G., T.J. Lo, T. Yucel, Q. Lu, and D.L. Kaplan, *Electrogelation for protein adhesives.* Advanced Materials, 2009. **22**(6): p. 711-715.
5. Mcgrath, K. and D. Kaplan, *Protein-based materials*1997: Birkhäuser.
6. Wang, X., J.A. Kluge, G.G. Leisk, and D.L. Kaplan, *Sonication-induced gelation of silk fibroin for cell encapsulation.* Biomaterials, 2008. **29**(8): p. 1054-1064.
7. Yucel, T., P. Cebe, and D.L. Kaplan, *Vortex-induced injectable silk fibroin hydrogels.* Biophysical journal, 2009. **97**(7): p. 2044-2050.
8. Meinel, L., S. Hofmann, V. Karageorgiou, L. Zichner, R. Langer, D. Kaplan, and G. Vunjak‐Novakovic, *Engineering cartilage‐like tissue using human mesenchymal stem cells and silk protein scaffolds.* Biotechnology and bioengineering, 2004. **88**(3): p. 379-391.
9. Nazarov, R., H.J. Jin, and D.L. Kaplan, *Porous 3-D scaffolds from regenerated silk fibroin.* Biomacromolecules, 2004. **5**(3): p. 718-726.
10. Karageorgiou, V. and D. Kaplan, *Porosity of 3D biomaterial scaffolds and osteogenesis.* Biomaterials, 2005. **26**(27): p. 5474-5491.
11. Kim, U.J., J. Park, H. Joo Kim, M. Wada, and D.L. Kaplan, *Three-dimensional aqueous-derived biomaterial scaffolds from silk fibroin.* Biomaterials, 2005. **26**(15): p. 2775-2785.
12. Wang, Y., U.J. Kim, D.J. Blasioli, H.J. Kim, and D.L. Kaplan, *In vitro cartilage tissue engineering with 3D porous aqueous-derived silk scaffolds and mesenchymal stem cells.* Biomaterials, 2005. **26**(34): p. 7082-7094.
13. Wang, Y., D.J. Blasioli, H.J. Kim, H.S. Kim, and D.L. Kaplan, *Cartilage tissue engineering with silk scaffolds and human articular chondrocytes.* Biomaterials, 2006. **27**(25): p. 4434-4442.
14. Hofmann, S., H. Hagenmüller, A.M. Koch, R. Müller, G. Vunjak-Novakovic, D.L. Kaplan, H.P. Merkle, and L. Meinel, *Control of in vitro tissue-engineered bone-like structures using human mesenchymal stem cells and porous silk scaffolds.* Biomaterials, 2007. **28**(6): p. 1152-1162.
15. Wang, Y., D.D. Rudym, A. Walsh, L. Abrahamsen, H.J. Kim, H.S. Kim, C. Kirker-Head, and D.L. Kaplan, *< i> In vivo</i> degradation of three-dimensional silk fibroin scaffolds.* Biomaterials, 2008. **29**(24): p. 3415-3428.
16. Sofia, S., M.B. Mccarthy, G. Gronowicz, and D.L. Kaplan, *Functionalized silk‐based biomaterials for bone formation.* Journal of biomedical materials research, 2000. **54**(1): p. 139-148.

17. Meinel, L., S. Hofmann, V. Karageorgiou, C. Kirker-Head, J. Mccool, G. Gronowicz, L. Zichner, R. Langer, G. Vunjak-Novakovic, and D.L. Kaplan, *The inflammatory responses to silk films in vitro and in vivo.* Biomaterials, 2005. **26**(2): p. 147-155.
18. Wang, X., X. Zhang, J. Castellot, I. Herman, M. Iafrati, and D.L. Kaplan, *Controlled release from multilayer silk biomaterial coatings to modulate vascular cell responses.* Biomaterials, 2008. **29**(7): p. 894-903.
19. Lu, S., X. Wang, Q. Lu, X. Hu, N. Uppal, F.G. Omenetto, and D.L. Kaplan, *Stabilization of enzymes in silk films.* Biomacromolecules, 2009. **10**(5): p. 1032-1042.
20. Lu, Q., X. Wang, X. Hu, P. Cebe, F. Omenetto, and D.L. Kaplan, *Stabilization and release of enzymes from silk films.* Macromolecular bioscience, 2010. **10**(4): p. 359-368.
21. Zhang, J., E. Pritchard, X. Hu, T. Valentin, B. Panilaitis, F.G. Omenetto, and D.L. Kaplan, *Stabilization of vaccines and antibiotics in silk and eliminating the cold chain.* Proceedings of the National Academy of Sciences, 2012. **109**(30): p. 11981-11986.
22. Jin, H.J., J. Park, V. Karageorgiou, U.J. Kim, R. Valluzzi, P. Cebe, and D.L. Kaplan, *Water‐Stable Silk Films with Reduced β‐Sheet Content.* Advanced Functional Materials, 2005. **15**(8): p. 1241-1247.
23. Kim, U.J., J. Park, C. Li, H.J. Jin, R. Valluzzi, and D.L. Kaplan, *Structure and properties of silk hydrogels.* Biomacromolecules, 2004. **5**(3): p. 786-792.
24. Wang, Y., H.J. Kim, G. Vunjak-Novakovic, and D.L. Kaplan, *Stem cell-based tissue engineering with silk biomaterials.* Biomaterials, 2006. **27**(36): p. 6064-6082.
25. Chao, P.H.G., S. Yodmuang, X. Wang, L. Sun, D.L. Kaplan, and G. Vunjak‐Novakovic, *Silk hydrogel for cartilage tissue engineering.* Journal of Biomedical Materials Research Part B: Applied Biomaterials, 2010. **95**(1): p. 84-90.
26. Guziewicz, N., A. Best, B. Perez-Ramirez, and D.L. Kaplan, *Lyophilized silk fibroin hydrogels for the sustained local delivery of therapeutic monoclonal antibodies.* Biomaterials, 2011. **32**(10): p. 2642-2650.
27. Zhang, W., X. Wang, S. Wang, J. Zhao, L. Xu, C. Zhu, D. Zeng, J. Chen, Z. Zhang, and D.L. Kaplan, *The use of injectable sonication-induced silk hydrogel for VEGF< sub> 165</sub> and BMP-2 delivery for elevation of the maxillary sinus floor.* Biomaterials, 2011. **32**(35): p. 9415-9424.
28. Jin, H.J., J. Chen, V. Karageorgiou, G.H. Altman, and D.L. Kaplan, *Human bone marrow stromal cell responses on electrospun silk fibroin mats.* Biomaterials, 2004. **25**(6): p. 1039-1047.
29. Wang, A.Y., P.D. Peng, A. Ehrhardt, T.A. Storm, and M.A. Kay, *Comparison of adenoviral and adeno-associated viral vectors for pancreatic gene delivery in vivo.* Human Gene Therapy, 2004. **15**(4): p. 405-413.
30. Li, C., C. Vepari, H.J. Jin, H.J. Kim, and D.L. Kaplan, *Electrospun silk-BMP-2 scaffolds for bone tissue engineering.* Biomaterials, 2006. **27**(16): p. 3115-3124.

31. Soffer, L., X. Wang, X. Zhang, J. Kluge, L. Dorfmann, D.L. Kaplan, and G. Leisk, *Silk-based electrospun tubular scaffolds for tissue-engineered vascular grafts.* Journal of Biomaterials Science, Polymer Edition, 2008. **19**(5): p. 653-664.
32. Zhang, X., C.B. Baughman, and D.L. Kaplan, *In vitro evaluation of electrospun silk fibroin scaffolds for vascular cell growth.* Biomaterials, 2008. **29**(14): p. 2217-2227.
33. Schneider, A., X. Wang, D. Kaplan, J. Garlick, and C. Egles, *Biofunctionalized electrospun silk mats as a topical bioactive dressing for accelerated wound healing.* Acta biomaterialia, 2009. **5**(7): p. 2570-2578.
34. Zhang, X., M.R. Reagan, and D.L. Kaplan, *Electrospun silk biomaterial scaffolds for regenerative medicine.* Advanced drug delivery reviews, 2009. **61**(12): p. 988-1006.
35. Wang, X., E. Wenk, A. Matsumoto, L. Meinel, C. Li, and D.L. Kaplan, *Silk microspheres for encapsulation and controlled release.* Journal of controlled release, 2007. **117**(3): p. 360-370.
36. Wang, X., T. Yucel, Q. Lu, X. Hu, and D.L. Kaplan, *Silk nanospheres and microspheres from silk/pva blend films for drug delivery.* Biomaterials, 2010. **31**(6): p. 1025-1035.
37. Wilz, A., E.M. Pritchard, T. Li, J.Q. Lan, D.L. Kaplan, and D. Boison, *Silk polymer-based adenosine release: therapeutic potential for epilepsy.* Biomaterials, 2008. **29**(26): p. 3609-3616.
38. Lammel, A.S., X. Hu, S.H. Park, D.L. Kaplan, and T.R. Scheibel, *Controlling silk fibroin particle features for drug delivery.* Biomaterials, 2010. **31**(16): p. 4583-4591.
39. Szybala, C., E.M. Pritchard, T.A. Lusardi, T. Li, A. Wilz, D.L. Kaplan, and D. Boison, *Antiepileptic effects of silk-polymer based adenosine release in kindled rats.* Experimental neurology, 2009. **219**(1): p. 126.
40. Horan, R.L., K. Antle, A.L. Collette, Y. Wang, J. Huang, J.E. Moreau, V. Volloch, D.L. Kaplan, and G.H. Altman, *In vitro degradation of silk fibroin.* Biomaterials, 2005. **26**(17): p. 3385-3393.
41. Li, M., M. Ogiso, and N. Minoura, *Enzymatic degradation behavior of porous silk fibroin sheets.* Biomaterials, 2003. **24**(2): p. 357-365.
42. Murray, C. and A. Lopez, *The global burden of disease and injury series, volume 1: a comprehensive assessment of mortality and disability from diseases, injuries, and risk factors in 1990 and projected to 2020.* Cambridge. MA, 1996.
43. Rutland-Brown, W., J.A. Langlois, K.E. Thomas, and Y.L. Xi, *Incidence of traumatic brain injury in the United States, 2003.* The Journal of head trauma rehabilitation, 2006. **21**(6): p. 544.
44. Langlois, J.A., W. Rutland-Brown, and M.M. Wald, *The epidemiology and impact of traumatic brain injury: a brief overview.* The Journal of head trauma rehabilitation, 2006. **21**(5): p. 375.
45. Sosin, D.M., J.E. Sniezek, and R.J. Waxweiler, *Trends in death associated with traumatic brain injury, 1979 through 1992.* JAMA: the journal of the American Medical Association, 1995. **273**(22): p. 1778-1780.

46. Hoge, C.W., D. Mcgurk, J.L. Thomas, A.L. Cox, C.C. Engel, and C.A. Castro, *Mild traumatic brain injury in US soldiers returning from Iraq.* New England Journal of Medicine, 2008. **358**(5): p. 453-463.
47. Finnie, J.W. and P.C. Blumbergs, *Animal Models: Traumatic Brain Injury.* Veterinary Pathology Online, 2002. **36**: p. 679-689.
48. Gurdjian, E., V. Roberts, and L. Thomas, *Tolerance curves of acceleration and intracranial pressure and protective index in experimental head injury.* The Journal of trauma, 1966. **6**(5): p. 600.
49. Kobrine, A. and L. Kempe, *Studies in head injury. I. An experimental model of closed head injury.* Surgical neurology, 1973. **1**(1): p. 34.
50. Ommaya, A.K., *Experimental head injury in the monkey.* Head injury. Philadelphia: Lippincott, 1966: p. 260-275.
51. Ommaya, A.K. and T. Gennarelli, *Cerebral concussion and traumatic unconsciousness.* Brain, 1974. **97**(1): p. 633-654.
52. Ommaya, A., T. Gennarelli, K. Sano, and S. Ishii, *Correlation between the biomechanics and pathophysiology of head injury.* Neural Trauma. New York: American Elsevier, 1974: p. 275-289.
53. Sekino, H., N. Nakamura, R. Kanda, M. Yasue, H. Masuzawa, N. Aoyagi, K. Mii, H. Kohno, T. Sugimori, and M. Sugiura, *Experimental head injury in monkeys using rotational acceleration impact (author's transl)].* Neurologia medico-chirurgica, 1980. **20**(2): p. 127.
54. Finnie, J.W., *Animal models of traumatic brain injury: a review.* Australian veterinary journal, 2001. **79**(9): p. 628-633.
55. Finnie, J.W., J. Manavis, P.C. Blumbergs, and G. Summersides, *Brain damage in sheep from penetrating captive bolt stunning.* Australian veterinary journal, 2002. **80**(1): p. 67-69.
56. Finnie, J., C. Van Den Heuvel, V. Gebski, J. Manavis, G. Summersides, and P. Blumbergs, *Effect of impact on different regions of the head of lambs.* Journal of comparative pathology, 2001. **124**(2-3): p. 159-164.
57. Lewis, S.B., J.W. Finnie, P.C. Blumbergs, G. Scott, J. Manavis, C. Brown, P.L. Reilly, N.R. Jones, and A. Mclean, *A head impact model of early axonal injury in the sheep.* Journal of neurotrauma, 1996. **13**(9): p. 505-514.
58. Tornheim, P.A., B.H. Liwnicz, C.S. Hirsch, D.L. Brown, and R.L. Mclaurin, *Acute responses to blunt head trauma.* Journal of neurosurgery, 1983. **59**(3): p. 431-438.
59. Bakay, L., J.C. Lee, G.C. Lee, and J.R. Peng, *Experimental cerebral concussion.* Journal of neurosurgery, 1977. **47**(4): p. 525-531.
60. Marmarou, A. and K. Shima, *Comparative studies of edema produced by fluid percussion injury with lateral and central modes of injury in cats.* Advances in neurology, 1990. **52**: p. 233.
61. Shapira, Y., E. Shohami, A. Sidi, D. Soffer, S. Freeman, and S. Cotev, *Experimental closed head injury in rats: mechanical, pathophysiologic, and neurologic properties.* Critical care medicine, 1988. **16**(3): p. 258.
62. Whalen, M.J., R.S.B. Clark, C.E. Dixon, P. Robichaud, D.W. Marion, V. Vagni, S.H. Graham, L. Virag, G. Hasko, and R. Stachlewitz, *Reduction of cognitive and motor deficits after traumatic brain injury in mice deficient in poly (ADP-*

ribose) polymerase. Journal of Cerebral Blood Flow & Metabolism, 1999. **19**(8): p. 835-842.
63. Whalen, M.J., T.M. Carlos, C.E. Dixon, P. Robichaud, R.S.B. Clark, D.W. Marion, and P.M. Kochanek, *Reduced brain edema after traumatic brain injury in mice deficient in P-selectin and intercellular adhesion molecule-1.* Journal of Leukocyte Biology, 2000. **67**(2): p. 160-168.
64. Qiu, J., M.J. Whalen, P. Lowenstein, G. Fiskum, B. Fahy, R. Darwish, B. Aarabi, J. Yuan, and M.A. Moskowitz, *Upregulation of the Fas receptor death-inducing signaling complex after traumatic brain injury in mice and humans.* The Journal of neuroscience, 2002. **22**(9): p. 3504-3511.
65. Yoshimura, S., T. Teramoto, M.J. Whalen, M.C. Irizarry, Y. Takagi, J. Qiu, J. Harada, C. Waeber, X.O. Breakefield, and M.A. Moskowitz, *FGF-2 regulates neurogenesis and degeneration in the dentate gyrus after traumatic brain injury in mice.* Journal of Clinical Investigation, 2003. **112**(8): p. 1202-1210.
66. Bermpohl, D., Z. You, S.J. Korsmeyer, M.A. Moskowitz, and M.J. Whalen, *Traumatic brain injury in mice deficient in Bid: effects on histopathology and functional outcome.* Journal of Cerebral Blood Flow & Metabolism, 2005. **26**(5): p. 625-633.
67. Whalen, M.J., T.M. Carlos, C.E. Dixon, J.K. Schiding, R.S.B. Clark, E. Baum, H.Q. Yan, D.W. Marion, and P.M. Kochanek, *Effect of traumatic brain injury in mice deficient in intercellular adhesion molecule–1: assessment of histopathologic and functional outcome.* Journal of neurotrauma, 1999. **16**(4): p. 299-309.
68. Gutierrez, E., Y. Huang, K. Haglid, F. Bao, H.A. Hansson, A. Hamberger, and D. Viano, *A new model for diffuse brain injury by rotational acceleration: I. Model, gross appearance, and astrocytosis.* Journal of neurotrauma, 2001. **18**(3): p. 247-257.
69. Adams, J.H., D. Graham, L.S. Murray, and G. Scott, *Diffuse axonal injury due to nonmissile head injury in humans: an analysis of 45 cases.* Annals of neurology, 1982. **12**(6): p. 557-563.
70. Adams, J.H., D. Doyle, I. Ford, T. Gennarelli, D. Graham, and D. Mclellan, *Diffuse axonal injury in head injury: definition, diagnosis and grading.* Histopathology, 1989. **15**(1): p. 49-59.
71. Meythaler, J.M., J.D. Peduzzi, E. Eleftheriou, and T.A. Novack, *Current concepts: Diffuse axonal injury [ndash] associated traumatic brain injury.* Archives of physical medicine and rehabilitation, 2001. **82**(10): p. 1461-1471.
72. Ommaya, A.K., A. Hirsch, E. Flamm, and R. Mahone, *Cerebral concussion in the monkey: an experimental model.* Science, 1966. **153**(3732): p. 211-212.
73. Ommaya, A. and A. Hirsch, *Tolerances for cerebral concussion from head impact and whiplash in primates.* Journal of Biomechanics, 1971. **4**(1): p. 13-21.
74. Ommaya, A.K., P. Corrao, and F.S. Letcher, *Head injury in the chimpanzee.* Journal of neurosurgery, 1973. **39**(2): p. 152-166.
75. Gennarelli, T.A., L.E. Thibault, J.H. Adams, D.I. Graham, C.J. Thompson, and R.P. Marcincin, *Diffuse axonal injury and traumatic coma in the primate.* Annals of neurology, 1982. **12**(6): p. 564-574.

76. Gennarelli, T.A. and L.E. Thibault, *Biological models of head injury.* Central Nervous System Trauma Status Report. Bethesda, Md: National Institute of Neurological and Communicative Disorders and Stroke, NIH, 1985: p. 391-404.
77. Gennarelli, T., L. Thibault, D. Ross, and D. Meaney, *Enhancement of axonal damage in the forebrain during contralateral cranectomy during controlled cortical impact injury in the rat.* Proceedings of the Society for Neuroscience, 1990. **15**.
78. Friess, S.H., R.N. Ichord, J. Ralston, K. Ryall, M.A. Helfaer, C. Smith, and S.S. Margulies, *Repeated traumatic brain injury affects composite cognitive function in piglets.* Journal of neurotrauma, 2009. **26**(7): p. 1111-1121.
79. Smith, D.H., K.I.M.M. Cecil, D.F. Meaney, X.H.a.N. Chen, T.K. Mcintosh, T.A. Gennarelli, and R.E. Lenkineki, *Magnetic resonance spectroscopy of diffuse brain trauma in the pig.* Journal of neurotrauma, 1998. **15**(9): p. 665-674.
80. Browne, K.D., X.H. Chen, D.F. Meaney, and D.H. Smith, *Mild Traumatic Brain Injury and Diffuse Axonal Injury in Swine.* Journal of neurotrauma, 2011. **28**(9): p. 1747-1755.
81. Nelson, L., E. Auen, R. Bourke, and K. Barron, *A new head injury model for evaluation of treatment modalities.* Neurosci Abst, 1979. **5**: p. 516.
82. Marmarou, A., M.a.a.E. Foda, W. Brink, J. Campbell, H. Kita, and K. Demetriadou, *A new model of diffuse brain injury in rats.* Journal of neurosurgery, 1994. **80**(2): p. 291-300.
83. Abd-Elfattah Foda, M.A. and A. Marmarou, *A new model of diffuse brain injury in rats.* Journal of neurosurgery, 1994. **80**(2): p. 301-313.
84. Heath, D.L. and R. Vink, *Improved motor outcome in response to magnesium therapy received up to 24 hours after traumatic diffuse axonal brain injury in rats.* Journal of neurosurgery, 1999. **90**(3): p. 504-509.
85. Xiao-Sheng, H., Y. Sheng-Yu, Z. Xiang, F. Zhou, Z. Jian-Ning, and Y. Li-Sun, *Diffuse axonal injury due to lateral head rotation in a rat model.* Journal of neurosurgery, 2000. **93**(4): p. 626-633.
86. Fijalkowski, R.J., B.D. Stemper, F.A. Pintar, N. Yoganandan, M.J. Crowe, and T.A. Gennarelli, *New rat model for diffuse brain injury using coronal plane angular acceleration.* Journal of neurotrauma, 2007. **24**(8): p. 1387-1398.
87. Gennarelli, T., *Head injury in man and experimental animals: clinical aspects.* Acta neurochirurgica. Supplementum, 1983. **32**: p. 1.
88. Gennarelli, T.A., *Animate models of human head injury.* Journal of neurotrauma, 1994. **11**(4): p. 357-368.
89. Chen, Z.J., W.C. Broaddus, R.R. Viswanathan, R. Raghavan, and G.T. Gillies, *Intraparenchymal drug delivery via positive-pressure infusion: experimental and modeling studies of poroelasticity in brain phantom gels.* Biomedical Engineering, IEEE Transactions on, 2002. **49**(2): p. 85-96.
90. Chen, Z.J., G.T. Gillies, W.C. Broaddus, S.S. Prabhu, H. Fillmore, R.M. Mitchell, F.D. Corwin, and P.P. Fatouros, *A realistic brain tissue phantom for intraparenchymal infusion studies.* Journal of neurosurgery, 2004. **101**(2): p. 314-322.

91. Hoffmann, R., T. Stieglitz, N. Hosseini, S. Kisban, O. Paul, and P. Ruther. *Comparative study on the insertion behavior of cerebral microprobes*. 2007. IEEE.
92. Panse, S., H. Fillmore, Z. Chen, G. Gillies, and W. Broaddus, *A novel coaxial tube catheter for central nervous system infusions: performance characteristics in brain phantom gel.* Journal of Medical Engineering & Technology, 2010. **34**(7-8): p. 408-414.
93. Ritter, R.C., E.G. Quate, G.T. Gillies, M.S. Grady, M.A. Howard Iii, and W.C. Broaddus, *Measurement of friction on straight catheters in in vitro brain and phantom material.* Biomedical Engineering, IEEE Transactions on, 1998. **45**(4): p. 476-485.
94. Gillies, G., S. Allison, and B. Tissue, *Positive pressure infusion of fluorescent nanoparticles as a probe of the structure of brain phantom gelatins.* Nanotechnology, 2002. **13**: p. 484.
95. Bauman, M., G. Gillies, R. Raghavan, M. Brady, and C. Pedain, *Physical characterization of neurocatheter performance in a brain phantom gelatin with nanoscale porosity: steady-state and oscillatory flows.* Nanotechnology, 2004. **15**: p. 92.
96. Surry, K., H. Austin, A. Fenster, and T. Peters, *Poly (vinyl alcohol) cryogel phantoms for use in ultrasound and MR imaging.* Physics in medicine and biology, 2004. **49**: p. 5529.
97. Surry, K. and T. Peters. *A PVA-C brain phantom derived from a high quality 3D MR data set*. 2001. Springer.
98. Matsumoto, A., J. Chen, A.L. Collette, U.J. Kim, G.H. Altman, P. Cebe, and D.L. Kaplan, *Mechanisms of silk fibroin sol-gel transitions.* The Journal of Physical Chemistry B, 2006. **110**(43): p. 21630-21638.
99. Lu, Q., Y. Huang, M. Li, B. Zuo, S. Lu, J. Wang, H. Zhu, and D.L. Kaplan, *Silk fibroin electrogelation mechanisms.* Acta Biomaterialia, 2011.
100. Mandal, B.B. and S.C. Kundu, *Biospinning by silkworms: Silk fiber matrices for tissue engineering applications.* Acta biomaterialia, 2010. **6**(2): p. 360-371.
101. Sofia, S., M.B. Mccarthy, G. Gronowicz, and D.L. Kaplan, *Functionalized silk‐based biomaterials for bone formation.* Journal of biomedical materials research, 2001. **54**(1): p. 139-148.
102. Jin, H.J. and D.L. Kaplan, *Mechanism of silk processing in insects and spiders.* Nature, 2003. **424**(6952): p. 1057-1061.
103. Lawrence, B.D., F. Omenetto, K. Chui, and D.L. Kaplan, *Processing methods to control silk fibroin film biomaterial features.* Journal of materials science, 2008. **43**(21): p. 6967-6985.
104. Lu, Q., X. Hu, X. Wang, J.A. Kluge, S. Lu, P. Cebe, and D.L. Kaplan, *Water-insoluble silk films with silk I structure.* Acta Biomaterialia, 2010. **6**(4): p. 1380-1387.
105. Jin, H.J., J. Park, V. Karageorgiou, U.J. Kim, R. Valluzzi, P. Cebe, and D.L. Kaplan, *Water-Stable Silk Films with Reduced β-Sheet Content.* Advanced Functional Materials, 2005. **15**(8): p. 1241-1247.

106. Anderson, R.W.G., C.J. Brown, P.C. Blumbergs, A.J. Mclean, and N.R. Jones, *Impact mechanics and axonal injury in a sheep model.* Journal of neurotrauma, 2003. **20**(10): p. 961-974.
107. Smith, D.H., M. Nonaka, R. Miller, M. Leoni, X.H. Chen, D. Alsop, and D.F. Meaney, *Immediate coma following inertial brain injury dependent on axonal damage in the brainstem.* Journal of neurosurgery, 2000. **93**(2): p. 315-322.
108. Raghupathi, R. and S.S. Margulies, *Traumatic axonal injury after closed head injury in the neonatal pig.* Journal of neurotrauma, 2002. **19**(7): p. 843-853.
109. Whalen, M.J., T.M. Carlos, P.M. Kochanek, R.S.B. Clark, S. Heineman, J.K. Schiding, D. Franicola, F. Memarzadeh, W. Lo, and D.W. Marion, *Neutrophils do not mediate blood-brain barrier permeability early after controlled cortical impact in rats.* Journal of neurotrauma, 1999. **16**(7): p. 583-594.
110. Bermpohl, D., Z. You, E.H. Lo, H.H. Kim, and M.J. Whalen, *TNF alpha and Fas mediate tissue damage and functional outcome after traumatic brain injury in mice.* Journal of Cerebral Blood Flow & Metabolism, 2007. **27**(11): p. 1806-1818.
111. Whalen, M.J., T. Dalkara, Z. You, J. Qiu, D. Bermpohl, N. Mehta, B. Suter, P.G. Bhide, E.H. Lo, and M. Ericsson, *Acute plasmalemma permeability and protracted clearance of injured cells after controlled cortical impact in mice.* Journal of Cerebral Blood Flow & Metabolism, 2007. **28**(3): p. 490-505.
112. You, Z., J. Yang, K. Takahashi, P.H. Yager, H.H. Kim, T. Qin, G.L. Stahl, R.a.B. Ezekowitz, M.C. Carroll, and M.J. Whalen, *Reduced tissue damage and improved recovery of motor function after traumatic brain injury in mice deficient in complement component C4.* Journal of Cerebral Blood Flow & Metabolism, 2007. **27**(12): p. 1954-1964.
113. Yu, S., Y. Kaneko, E. Bae, C.E. Stahl, Y. Wang, H. Van Loveren, P.R. Sanberg, and C.V. Borlongan, *Severity of controlled cortical impact traumatic brain injury in rats and mice dictates degree of behavioral deficits.* Brain research, 2009. **1287**: p. 157-163.
114. Hitomi, J., D.E. Christofferson, A. Ng, J. Yao, A. Degterev, R.J. Xavier, and J. Yuan, *Identification of a molecular signaling network that regulates a cellular necrotic cell death pathway.* Cell, 2008. **135**(7): p. 1311-1323.
115. Degterev, A., J. Hitomi, M. Germscheid, I.L. Ch'en, O. Korkina, X. Teng, D. Abbott, G.D. Cuny, C. Yuan, and G. Wagner, *Identification of RIP1 kinase as a specific cellular target of necrostatins.* Nature chemical biology, 2008. **4**(5): p. 313-321.
116. Degterev, A., Z. Huang, M. Boyce, Y. Li, P. Jagtap, N. Mizushima, G.D. Cuny, T.J. Mitchison, M.A. Moskowitz, and J. Yuan, *Chemical inhibitor of nonapoptotic cell death with therapeutic potential for ischemic brain injury.* Nature chemical biology, 2005. **1**(2): p. 112-119.
117. Smith, C.C.T., S.M. Davidson, S.Y. Lim, J.C. Simpkin, J.S. Hothersall, and D.M. Yellon, *Necrostatin: a potentially novel cardioprotective agent?* Cardiovascular Drugs and Therapy, 2007. **21**(4): p. 227-233.
118. Hofmann, S., C. Wong Po Foo, F. Rossetti, M. Textor, G. Vunjak-Novakovic, D. Kaplan, H. Merkle, and L. Meinel, *Silk fibroin as an organic polymer for*

controlled drug delivery. Journal of controlled release, 2006. **111**(1): p. 219-227.
119. Karageorgiou, V., M. Tomkins, R. Fajardo, L. Meinel, B. Snyder, K. Wade, J. Chen, G. Vunjak‐Novakovic, and D.L. Kaplan, *Porous silk fibroin 3‐D scaffolds for delivery of bone morphogenetic protein‐2 in vitro and in vivo.* Journal of Biomedical Materials Research Part A, 2006. **78**(2): p. 324-334.
120. Numata, K. and D.L. Kaplan, *Silk-based delivery systems of bioactive molecules.* Advanced drug delivery reviews, 2010. **62**(15): p. 1497-1508.
121. Pritchard, E.M. and D.L. Kaplan, *Silk fibroin biomaterials for controlled release drug delivery.* Expert Opinion on Drug Delivery, 2011. **8**(6): p. 797-811.
122. Xu, X., C.C. Chua, J. Kong, R.M. Kostrzewa, U. Kumaraguru, R.C. Hamdy, and B.H.L. Chua, *Necrostatin‐1 protects against glutamate‐induced glutathione depletion and caspase‐independent cell death in HT‐22 cells.* Journal of neurochemistry, 2007. **103**(5): p. 2004-2014.
123. You, Z., S.I. Savitz, J. Yang, A. Degterev, J. Yuan, G.D. Cuny, M.A. Moskowitz, and M.J. Whalen, *Necrostatin-1 reduces histopathology and improves functional outcome after controlled cortical impact in mice.* Journal of Cerebral Blood Flow & Metabolism, 2008. **28**(9): p. 1564-1573.
124. Han, W., J. Xie, L. Li, Z. Liu, and X. Hu, *Necrostatin-1 reverts shikonin-induced necroptosis to apoptosis.* Apoptosis, 2009. **14**(5): p. 674-686.
125. Northington, F.J., R. Chavez-Valdez, E.M. Graham, S. Razdan, E.B. Gauda, and L.J. Martin, *Necrostatin decreases oxidative damage, inflammation, and injury after neonatal HI.* Journal of Cerebral Blood Flow & Metabolism, 2010. **31**(1): p. 178-189.
126. Xu, X., K.W. Chua, C.C. Chua, C.F. Liu, R.C. Hamdy, and B.H.L. Chua, *Synergistic protective effects of humanin and necrostatin-1 on hypoxia and ischemia/reperfusion injury.* Brain research, 2010. **1355**: p. 189-194.
127. Zhu, S., Y. Zhang, G. Bai, and H. Li, *Necrostatin-1 ameliorates symptoms in R6/2 transgenic mouse model of Huntington's disease.* Cell death & disease, 2011. **2**(1): p. e115.
128. Vandenabeele, P., L. Galluzzi, T.V. Berghe, and G. Kroemer, *Molecular mechanisms of necroptosis: an ordered cellular explosion.* Nature Reviews Molecular Cell Biology, 2010. **11**(10): p. 700-714.
129. Maki, J.L., E.E. Smith, X. Teng, S.S. Ray, G.D. Cuny, and A. Degterev, *Fluorescence polarization assay for inhibitors of the kinase domain of receptor interacting protein 1.* Analytical Biochemistry, 2012.
130. Krishan, A., *Rapid flow cytofluorometric analysis of mammalian cell cycle by propidium iodide staining.* The Journal of cell biology, 1975. **66**(1): p. 188-193.
131. Kuypers, H., M. Bentivoglio, D. Van Der Kooy, and C. Catsman-Berrevoets, *Retrograde transport of bisbenzimide and propidium iodide through axons to their parent cell bodies.* Neuroscience letters, 1979. **12**(1): p. 1-7.
132. Jones, K.H. and J.A. Senft, *An improved method to determine cell viability by simultaneous staining with fluorescein diacetate-propidium iodide.* Journal of Histochemistry & Cytochemistry, 1985. **33**(1): p. 77-79.

133. Macklis, J.D. and R.D. Madison, *Progressive incorporation of propidium iodide in cultured mouse neurons correlates with declining electrophysiological status: a fluorescence scale of membrane integrity.* Journal of neuroscience methods, 1990. **31**(1): p. 43-46.
134. Bonfoco, E., D. Krainc, M. Ankarcrona, P. Nicotera, and S.A. Lipton, *Apoptosis and necrosis: two distinct events induced, respectively, by mild and intense insults with N-methyl-D-aspartate or nitric oxide/superoxide in cortical cell cultures.* Proceedings of the National Academy of Sciences, 1995. **92**(16): p. 7162-7166.
135. Wu, Z., A. Asokan, and R.J. Samulski, *Adeno-associated virus serotypes: vector toolkit for human gene therapy.* Molecular Therapy, 2006. **14**(3): p. 316-327.
136. Jenis, L., J. Wingard, and E. Terwilliger. *Demonstration of Bmp Inhibition By Noggin in An in Vivo Rodent Spinal Fusion Model: Differential Effects of Bmp‐7, Bmp‐6 and Mutated Bmp‐7: P72*. in *Spine Journal Meeting Abstracts*. 2011.
137. Ulrich-Vinther, M., E.E. Carmody, J.J. Goater, K. Sï, R.J. O'keefe, and E.M. Schwarz, *Recombinant adeno-associated virus-mediated osteoprotegerin gene therapy inhibits wear debris-induced osteolysis.* The Journal of Bone & Joint Surgery, 2002. **84**(8): p. 1405-1412.
138. Heldermon, C.D., K.K. Ohlemiller, E.D. Herzog, C. Vogler, E. Qin, D.F. Wozniak, Y. Tan, J.L. Orrock, and M.S. Sands, *Therapeutic efficacy of bone marrow transplant, intracranial AAV-mediated gene therapy, or both in the mouse model of MPS IIIB.* Molecular Therapy, 2010. **18**(5): p. 873-880.
139. Alaee, F., O. Sugiyama, M.S. Virk, Y. Tang, B. Wang, and J.R. Lieberman, *In vitro evaluation of a double-stranded self-complementary adeno-associated virus type2 vector in bone marrow stromal cells for bone healing.* Genetic vaccines and therapy, 2011. **9**(1): p. 4.
140. Su, H., J. Takagawa, Y. Huang, J. Arakawa-Hoyt, J. Pons, W. Grossman, and Y.W. Kan, *Additive effect of AAV-mediated angiopoietin-1 and VEGF expression on the therapy of infarcted heart.* International journal of cardiology, 2009. **133**(2): p. 191-197.
141. Park, C.S., H. Cha, E.J. Kwon, D. Jeong, R.J. Hajjar, E.G. Kranias, C. Cho, and W.J. Park, *AAV-Mediated Knock-Down of HRC Exacerbates Transverse Aorta Constriction-Induced Heart Failure.* PloS one, 2012. **7**(8): p. e43282.
142. Wang, Z., T. Zhu, C. Qiao, L. Zhou, B. Wang, J. Zhang, C. Chen, J. Li, and X. Xiao, *Adeno-associated virus serotype 8 efficiently delivers genes to muscle and heart.* Nature biotechnology, 2005. **23**(3): p. 321-328.
143. Wang, L., R. Calcedo, H. Wang, P. Bell, R. Grant, L.H. Vandenberghe, J. Sanmiguel, H. Morizono, M.L. Batshaw, and J.M. Wilson, *The pleiotropic effects of natural AAV infections on liver-directed gene transfer in macaques.* Molecular Therapy, 2009. **18**(1): p. 126-134.
144. Wang, L., H. Wang, P. Bell, R.J. Mccarter, J. He, R. Calcedo, L.H. Vandenberghe, H. Morizono, M.L. Batshaw, and J.M. Wilson, *Systematic evaluation of AAV vectors for liver directed gene transfer in murine models.* Molecular Therapy, 2009. **18**(1): p. 118-125.

145. Nakai, H., S. Fuess, T.A. Storm, S. Muramatsu, Y. Nara, and M.A. Kay, *Unrestricted hepatocyte transduction with adeno-associated virus serotype 8 vectors in mice.* Journal of Virology, 2005. **79**(1): p. 214-224.
146. Thomas, C.E., T.A. Storm, Z. Huang, and M.A. Kay, *Rapid uncoating of vector genomes is the key to efficient liver transduction with pseudotyped adeno-associated virus vectors.* Journal of Virology, 2004. **78**(6): p. 3110-3122.
147. Takeda, S., M. Takahashi, H. Mizukami, E. Kobayashi, K. Takeuchi, Y. Hakamata, T. Kaneko, H. Yamamoto, C. Ito, and K. Ozawa, *Successful gene transfer using adeno-associated virus vectors into the kidney: comparison among adeno-associated virus serotype 1–5 vectors in vitro and in vivo.* Nephron Experimental Nephrology, 2004. **96**(4): p. e119-e126.
148. Lipkowitz, M.S., B. Hanss, N. Tulchin, P.D. Wilson, J.C. Langer, M.D. Ross, G.J. Kurtzman, P.E. Klotman, and M.E. Klotman, *Transduction of renal cells in vitro and in vivo by adeno-associated virus gene therapy vectors.* Journal of the American Society of Nephrology, 1999. **10**(9): p. 1908-1915.
149. Imai, E. and Y. Isaka, *Strategies of gene transfer to the kidney.* Kidney international, 1998. **53**(2): p. 264-272.
150. Limberis, M.P., L.H. Vandenberghe, L. Zhang, R.J. Pickles, and J.M. Wilson, *Transduction efficiencies of novel AAV vectors in mouse airway epithelium in vivo and human ciliated airway epithelium in vitro.* Molecular Therapy, 2008. **17**(2): p. 294-301.
151. Li, W., L. Zhang, J.S. Johnson, W. Zhijian, J.C. Grieger, X. Ping-Jie, L.M. Drouin, M. Agbandje-Mckenna, R.J. Pickles, and R.J. Samulski, *Generation of novel AAV variants by directed evolution for improved CFTR delivery to human ciliated airway epithelium.* Molecular Therapy, 2009. **17**(12): p. 2067-2077.
152. Darrick, L.Y., N.M. Linnerth-Petrik, C.L. Halbert, S.R. Walsh, A.D. Miller, and S.K. Wootton, *JSRV and ENTV Promoters Drive Gene Expression in All Airway Epithelial Cells of Mice but Only Induce Tumors in the Alveolar Region of the Lung.* Journal of Virology, 2011.
153. Buch, P., J. Bainbridge, and R. Ali, *AAV-mediated gene therapy for retinal disorders: from mouse to man.* Gene therapy, 2008. **15**(11): p. 849-857.
154. Ali, R.R., M.B. Reichel, A.J. Thrasher, R.J. Levinsky, C. Kinnon, N. Kanuga, D.M. Hunt, and S.S. Bhattacharya, *Gene transfer into the mouse retina mediated by an adeno-associated viral vector.* Human molecular genetics, 1996. **5**(5): p. 591-594.
155. Flannery, J.G., S. Zolotukhin, M.I. Vaquero, M.M. Lavail, N. Muzyczka, and W.W. Hauswirth, *Efficient photoreceptor-targeted gene expression in vivo by recombinant adeno-associated virus.* Proceedings of the National Academy of Sciences, 1997. **94**(13): p. 6916-6921.
156. Weber, M., J. Rabinowitz, N. Provost, H. Conrath, S. Folliot, D. Briot, Y. Chérel, P. Chenuaud, J. Samulski, and P. Moullier, *Recombinant adeno-associated virus serotype 4 mediates unique and exclusive long-term transduction of retinal pigmented epithelium in rat, dog, and nonhuman primate after subretinal delivery.* Molecular Therapy, 2003. **7**(6): p. 774-781.
157. Gao, G.P., M.R. Alvira, L. Wang, R. Calcedo, J. Johnston, and J.M. Wilson, *Novel adeno-associated viruses from rhesus monkeys as vectors for human gene*

therapy. Proceedings of the National Academy of Sciences, 2002. **99**(18): p. 11854-11859.
158. Gao, G., L.H. Vandenberghe, M.R. Alvira, Y. Lu, R. Calcedo, X. Zhou, and J.M. Wilson, *Clades of adeno-associated viruses are widely disseminated in human tissues.* Journal of Virology, 2004. **78**(12): p. 6381-6388.
159. Xiao, W., N. Chirmule, S.C. Berta, B. Mccullough, G. Gao, and J.M. Wilson, *Gene therapy vectors based on adeno-associated virus type 1.* Journal of Virology, 1999. **73**(5): p. 3994-4003.
160. Blankinship, M.J., P. Gregorevic, J.M. Allen, S.Q. Harper, H. Harper, C.L. Halbert, D.A. Miller, and J.S. Chamberlain, *Efficient transduction of skeletal muscle using vectors based on adeno-associated virus serotype 6.* Molecular Therapy, 2004. **10**(4): p. 671-678.
161. Chao, H., Y. Liu, J. Rabinowitz, C. Li, R.J. Samulski, and C.E. Walsh, *Several log increase in therapeutic transgene delivery by distinct adeno-associated viral serotype vectors.* Molecular Therapy, 2000. **2**(6): p. 619-623.
162. Prabhakar, S., M. Taherian, D. Gianni, T. Conlon, G. Fulci, J. Brockmann, A. Stemmer-Rachamimov, M. Sena-Esteves, X.O. Breakefield, and G.J. Brenner, *Regression of Schwannomas Induced by AAV-Mediated Delivery of Caspase-1.* Human Gene Therapy, 2012(ja).
163. Mulcahy, P., A. O'doherty, A. Paucard, T. O'brien, D. Kirik, and E. Dowd, *Development and characterization of a novel rat model of Parkinson's disease induced by sequential intranigral administration of AAV-α-synuclein and the pesticide, rotenone.* Neuroscience, 2011.
164. Franich, N.R., H.L. Fitzsimons, D.M. Fong, M. Klugmann, M.J. During, and D. Young, *AAV Vector–mediated RNAi of Mutant Huntingtin Expression Is Neuroprotective in a Novel Genetic Rat Model of Huntington's Disease.* Molecular Therapy, 2008. **16**(5): p. 947-956.
165. Ramaswamy, S., J.L. Mcbride, I. Han, E.M. Berry-Kravis, L. Zhou, C.D. Herzog, M. Gasmi, R.T. Bartus, and J.H. Kordower, *Intrastriatal CERE-120 (AAV-Neurturin) protects striatal and cortical neurons and delays motor deficits in a transgenic mouse model of Huntington's disease.* Neurobiology of disease, 2009. **34**(1): p. 40-50.
166. Zuleta, A., R.L. Vidal, D. Armentano, G. Parsons, and C. Hetz, *AAV-mediated delivery of the transcription factor XBP1s locally into the striatum reduces mutant Huntingtin aggregation in a mouse model of Huntington's disease.* Biochemical and Biophysical Research Communications, 2012.
167. Meijer, D.H., C.A. Maguire, S.G. Leroy, and M. Sena-Esteves, *Controlling brain tumor growth by intraventricular administration of an AAV vector encoding IFN-β.* Cancer gene therapy, 2009. **16**(8): p. 664-671.
168. Niers, J.M., C. Maguire, M. Kerami, M. Broekman, B.A. Tannous, and M.S. Esteves, *Stromal derived factor 1 alpha acts as a magnet for glioblastoma.* NOVEL BIOSENSORS FOR PRECLINICAL BRAIN TUMOR ANALYSIS, 2011: p. 115.
169. Maguire, C.A., D. Gianni, D.H. Meijer, L.A. Shaket, H. Wakimoto, S.D. Rabkin, G. Gao, and M. Sena-Esteves, *Directed evolution of adeno-associated virus for glioma cell transduction.* Journal of neuro-oncology, 2010. **96**(3): p. 337-347.

170. Dodiya, H.B., T. Bjorklund, J. Stansell Iii, R.J. Mandel, D. Kirik, and J.H. Kordower, *Differential transduction following basal ganglia administration of distinct pseudotyped AAV capsid serotypes in nonhuman primates.* Molecular Therapy, 2009. **18**(3): p. 579-587.
171. Weinberg, M.S., R. Jude Samulski, and T.J. Mccown, *Adeno-associated virus (AAV) gene therapy for neurological disease.* Neuropharmacology, 2012.
172. Liu, Y., C. Studzinski, T. Beckett, H. Guan, M.A. Hersh, M.P. Murphy, R. Klein, and L.B. Hersh, *Expression of neprilysin in skeletal muscle reduces amyloid burden in a transgenic mouse model of Alzheimer disease.* Molecular Therapy, 2009. **17**(8): p. 1381-1386.
173. Kaplitt, M.G., A. Feigin, C. Tang, H.L. Fitzsimons, P. Mattis, P.A. Lawlor, R.J. Bland, D. Young, K. Strybing, and D. Eidelberg, *Safety and tolerability of gene therapy with an adeno-associated virus (AAV) borne< i> GAD</i> gene for Parkinson's disease: an open label, phase I trial.* The Lancet, 2007. **369**(9579): p. 2097-2105.
174. Hara, H., A. Monsonego, K. Yuasa, K. Adachi, X. Xiao, S. Takeda, K. Takahashi, H. Weiner, and T. Tabira, *Development of a safe oral Abeta vaccine using recombinant adeno-associated virus vector for Alzheimer's disease.* JOURNAL OF ALZHEIMERS DISEASE, 2004. **6**(5): p. 483-488.
175. Zhang, J., X. Wu, C. Qin, J. Qi, S. Ma, H. Zhang, Q. Kong, D. Chen, D. Ba, and W. He, *A novel recombinant adeno-associated virus vaccine reduces behavioral impairment and b-amyloid plaques in a mouse model of Alzheimer's disease.* Neurobiology of disease, 2003. **14**(3): p. 365-379.
176. Fukuchi, K., K. Tahara, H.D. Kim, J.A. Maxwell, T.L. Lewis, M.A. Accavitti-Loper, H. Kim, S. Ponnazhagan, and R. Lalonde, *Anti-Aβ single-chain antibody delivery via adeno-associated virus for treatment of Alzheimer's disease.* Neurobiology of disease, 2006. **23**(3): p. 502-511.
177. Loiler, S.A., Q. Tang, T. Clarke, M.L. Campbell-Thompson, V. Chiodo, W. Hauswirth, P. Cruz, M. Perret-Gentil, M.A. Atkinson, and V.K. Ramiya, *Localized gene expression following administration of adeno-associated viral vectors via pancreatic ducts.* Molecular Therapy, 2005. **12**(3): p. 519-527.
178. Karvinen, H., E. Pasanen, T. Rissanen, P. Korpisalo, E. Vähäkangas, A. Jazwa, M. Giacca, and S. Ylä-Herttuala, *Long-term VEGF-A expression promotes aberrant angiogenesis and fibrosis in skeletal muscle.* Gene therapy, 2011.
179. Varadi, K., S. Michelfelder, T. Korff, M. Hecker, M. Trepel, H. Katus, J. Kleinschmidt, and O. Müller, *Novel random peptide libraries displayed on AAV serotype 9 for selection of endothelial cell-directed gene transfer vectors.* Gene therapy, 2011.
180. Sun, H., T. Le, T.T.J. Chang, A. Habib, S. Wu, F. Shen, W.L. Young, H. Su, and J. Liu, *AAV-mediated netrin-1 overexpression increases peri-infarct blood vessel density and improves motor function recovery after experimental stroke.* Neurobiology of disease, 2011. **44**(1): p. 73-83.
181. Numata, K., B. Subramanian, H.A. Currie, and D.L. Kaplan, *Bioengineered silk protein-based gene delivery systems.* Biomaterials, 2009. **30**(29): p. 5775-5784.

182. Numata, K., J. Hamasaki, B. Subramanian, and D.L. Kaplan, *Gene delivery mediated by recombinant silk proteins containing cationic and cell binding motifs.* Journal of controlled release, 2010. **146**(1): p. 136-143.
183. Gray, S.J., B.L. Blake, H.E. Criswell, S.C. Nicolson, R.J. Samulski, and T.J. Mccown, *Directed evolution of a novel adeno-associated virus (AAV) vector that crosses the seizure-compromised blood–brain barrier (BBB).* Molecular Therapy, 2009. **18**(3): p. 570-578.
184. Manfredsson, F.P., A.C. Rising, and R.J. Mandel, *AAV9: a potential blood-brain barrier buster.* Molecular Therapy, 2009. **17**(3): p. 403-405.
185. Fu, H., J. Dirosario, S. Killedar, K. Zaraspe, and D.M. Mccarty, *Correction of neurological disease of mucopolysaccharidosis IIIB in adult mice by rAAV9 trans-blood–brain barrier gene delivery.* Molecular Therapy, 2011. **19**(6): p. 1025-1033.
186. Saunders, N.R., C.J. Ek, and K.M. Dziegielewska, *The neonatal blood-brain barrier is functionally effective, and immaturity does not explain differential targeting of AAV9.* Nature biotechnology, 2009. **27**(9): p. 804-805.
187. Di Pasquale, G. and J.A. Chiorini, *AAV transcytosis through barrier epithelia and endothelium.* Molecular Therapy, 2006. **13**(3): p. 506-516.
188. Wright, J.F., T. Le, J. Prado, J. Bahr-Davidson, P.H. Smith, Z. Zhen, J.M. Sommer, G.F. Pierce, and G. Qu, *Identification of factors that contribute to recombinant AAV2 particle aggregation and methods to prevent its occurrence during vector purification and formulation.* Molecular Therapy, 2005. **12**(1): p. 171-178.